

DC-Net: Divide-and-Conquer for Salient Object Detection

Jiayi Zhu
MBZUAI
Abu Dhabi, UAE

zjyzhujiayi55@gmail.com

Xuebin Qin
MBZUAI
Abu Dhabi, UAE

xuebinua@gmail.com

Abdulmoteleb Elsaddik
MBZUAI
Abu Dhabi, UAE

a.elsaddik@mbzuai.ac.ae

Abstract

In this paper, to guide the model’s training process to explicitly present a progressive trend, we first introduce the concept of Divide-and-Conquer into Salient Object Detection (SOD) tasks, called DC-Net. Our DC-Net guides multiple encoders to solve different subtasks and then aggregates the feature maps with different semantic information obtained by multiple encoders into the decoder to predict the final saliency map. The decoder of DC-Net consists of newly designed two-level Residual nested-ASPP (ResASPP²) modules, which improve the sparse receptive field existing in ASPP and the disadvantage that the U-shape structure needs downsampling to obtain a large receptive field. Based on the advantage of Divide-and-Conquer’s parallel computing, we parallelize DC-Net through reparameterization, achieving competitive performance on six LR-SOD and five HR-SOD datasets under high efficiency (60 FPS and 55 FPS). Codes and results are available: <https://github.com/PiggyJerry/DC-Net>.

1. Introduction

Recently, with the development of deep convolutional neural networks (CNNs), downstream computer vision tasks have been greatly improved, and Salient Object Detection (SOD) has also benefited from it. The purpose of SOD is to segment the most visually attractive part of an image, and it is widely used in 3D modeling, image editing, art design materials, AR and 3D rendering. So what are the deficiencies worthy of researchers to explore? Next, we will discuss it based on the previous method.

In recent years, several deep salient object detection methods have introduced different auxiliary maps (e.g. edge maps, body maps, and detail maps) to assist in generating saliency maps, and their designs fall into the following three categories. First, after feeding the image into an encoder, use the features learned by predicting different auxiliary maps to assist in predicting the saliency maps [29, 72]. The second is to use auxiliary maps as input to guide the training

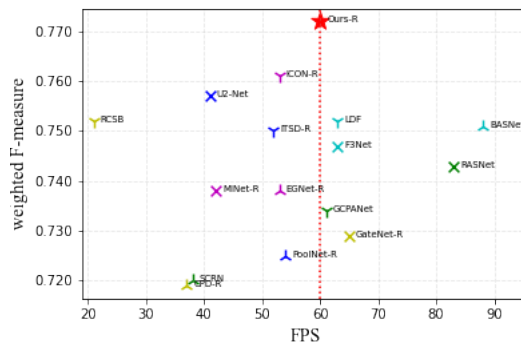


Figure 1. Comparison of FPS and performance of our DC-Net-R with other state-of-the-art SOD convolution-based methods. The F_{β}^w measure is computed on dataset DUT-OMRON [65]. The red star denotes our DC-Net-R (Ours-R, 60 FPS) and the red dot line denotes the real-time (60 FPS) line.

process [52]. The third is to make the models pay more attention to the edge pixels through the boundary-aware loss [46, 14]. However, these methods have some limitations. For the first method, a single encoder with multiple heads to learn different semantic information may not fully represent all the different semantic information [58, 60]. Moreover, when multiple branches need to interact with each other with a sequence, they cannot be accelerated through parallelism, leading to low efficiency [74]. The second method suffers from the need to generate auxiliary maps during the inference stage, leading to low efficiency. The third method can only use the boundary information. It is more intuitive and effective to directly use auxiliary maps for training. Moreover, most methods directly input the output feature maps of a single encoder into the decoder to predict the final saliency map. However, the output feature maps of a single encoder are a fusion of different features and cannot fully consider the quality of each feature.

This leads to our first question: **can we design an end-to-end network that explicitly guides the training process by using multiple encoders to represent the different semantic information of the saliency map to learn**

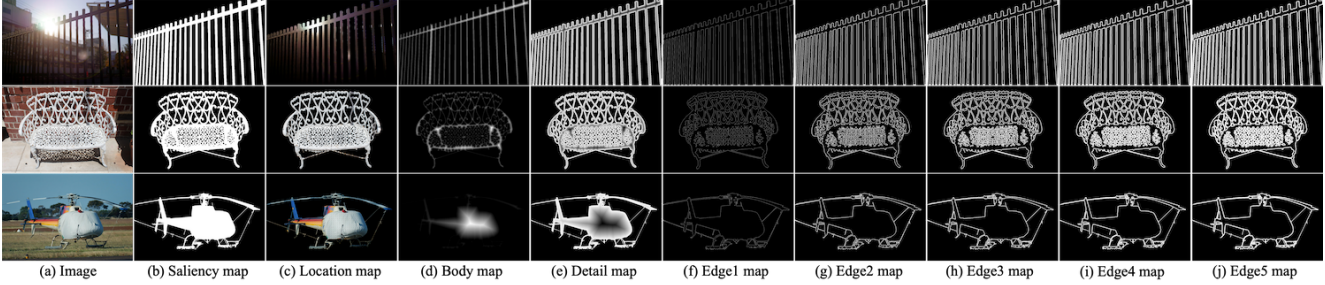


Figure 2. Some examples of different auxiliary maps. (c) represents the location information of the salient object. The sum of (d) and (e) is equal to (b). (f)-(j) represents the edge pixels of salient objects with widths 1, 2, 3, 4, and 5 respectively.

the prior knowledge before predicting the saliency map and be efficient?

Current mainstream pixel-level deep CNNs such as U-Net [47] and feature pyramid network (FPN) [28] increase the receptive field and improve efficiency through continuous pooling layers or convolutional layers with stride of 2, while pooling operation can lose detail information, that is, sacrifice the high resolution of the feature maps, and convolution with stride of 2 results in no convolution operation on half the pixels. Dilated convolution and atrous spatial pyramid pooling (ASPP) are proposed by Deeplab [3] for this problem, but due to the large gap in the atrous rate and only one parallel convolutional layer, the pixel sampling is sparse. A recently proposed method U²-Net [45] proposes a Residual U-blocks (RSU), and it can obtain multi-scale feature maps after several pooling layers at each stage, and finally restore to the high resolution of the current stage like U-Net, but the pooling operation still leads to the loss of detail information in this process.

Therefore, our second question is: **can we design a module to obtain a larger receptive field with fewer convolutional layers while maintaining the high resolution of the feature maps of the current stage all the time?**

Our main contribution is a novel method for SOD, called Divide-and-Conquer Network (**DC-Net**) with a two-level Residual nested-ASPP module (**ResASPP²**), which solves the two issues raised above, and we introduce **Parallel Acceleration** into DC-Net to speed it up. Our network training process is as follows: after feeding the image into two identical encoders, edge maps with width 4 and the location maps are used to supervise the two encoders respectively, as shown in Fig. 2 (i) and (c), and then the concatenation of the feature maps of the two encoders are fed into the decoder composed of ResASPP²s to predict the final saliency maps in the way of U-Net like structure. ResASPP² obtains a large and compact effective receptive field (ERF) without sacrificing high resolution by nesting two layers of parallel convolutional layers with dilation rates {1, 3, 5, 7}. Additionally, its output feature map has much diversity by fusing a large number of feature maps with different scales and compact pixel sampling. Parallel Acceleration merges two

identical encoders into an encoder with the same structure, which is called **Parallel Encoder**. ResASPP² is simplified by our implementation of **Merged Convolution**. Our DC-Net achieves competitive performance against the state-of-the-art (SOTA) methods on five public SOD datasets and runs at real-time (60 FPS based on **Parallel-ResNet-34**, with input size of $352 \times 352 \times 3$; 55 FPS based on **Parallel-ResNet-34**, with input size of $1024 \times 1024 \times 3$; 29 FPS based on **Parallel-Swin-B**, with input size of $384 \times 384 \times 3$) on a single RTX 6000 GPU.

2. Related Works

Under the increasing demand for higher efficiency and accuracy in the real world, traditional methods [17, 65, 34] based on hand-crafted features are gradually losing competitiveness. In recent years, more and more deep salient object detection networks [16, 69] have been proposed, and a lot of research has been done on how to integrate multi-level and multi-scale features [26], and how to use the auxiliary maps such as the edge map to train the network [72]. Recently, the emergence of SAM [21] and its variants, such as MedSAM [37] and HQ-SAM [18], has greatly facilitated the development of segmentation tasks. However, research on the aforementioned issues remains crucial for achieving better performance.

Multi-level and multi-scale feature integration: Recent works such as U-Net [47], Feature Pyramid Network (FPN) [28], PSPNet [71] and Deeplab [3] have shown that the fusion of multi-scale contextual features can lead to better results. Many subsequent developed methods for SOD to integrate or aggregate multi-level and multi-scale features were inspired by them to some extent. Liu *et al.* (Pool-Net) [29] aggregate the multi-scale features obtained from a module adapted from pyramid pooling module at each level of the decoder and a global guidance module is introduced to help each level obtain better location information. Wei *et al.* (F³Net) [57] propose a feature fusion strategy that is different from addition or concatenation, which can adaptively select fused features and reduce redundant information. Mohammadi *et al.* (CAGNet) [39] propose a multi-

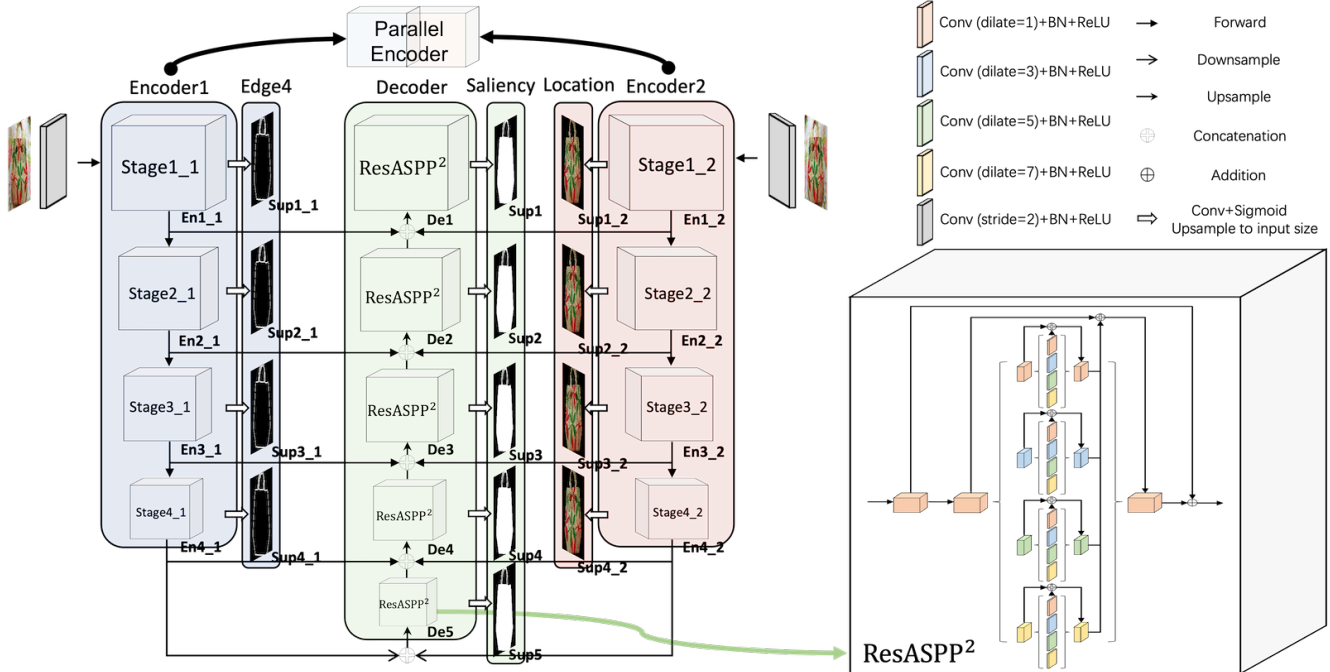


Figure 3. Illustration of our proposed DC-Net architecture. DC-Net has two encoders and a decoder, we can consider these two encoders as one parallel encoder. Thus, the main architecture of DC-Net is a U-Net like Encoder-Decoder, where each stage of the decoder consists of our newly proposed two-level Residual nested-ASPP module (ResASPP^2).

scale feature extraction module that combines convolutions with different sizes of convolution kernels in parallel. Zhao *et al.* (GateNet) [73] propose a Fold-ASPP module to generate finer multi-scale advanced saliency features. Zhuge *et al.* (ICON) [75] make full use of the features under various receptive fields to improve the diversity of features, and introduce an attention module to enhance feature channels that the integral salient objects are highlighted. Liu *et al.* (PiCANet) [30] generate global and local contextual attention for each pixel and use it on a U-Net structure. Li *et al.* [23] design a dynamic searching process module as a meta operation to conduct multi-scale and multi-modal feature fusion. Liu *et al.* (SMAC) [31] propose a novel mutual attention model by fusing attention and context from different modalities to better fuse cross-modal information. Fang *et al.* (DNTDF) [13] propose the progressive compression shortcut paths (PCSPs) to read features from higher levels. Zhang *et al.* [70] propose a multi-scale, multi-modal, and multi-level feature fusion module, leveraging the robustness of the thermal sensing modality to illumination and occlusion. Chen *et al.* (GCPANet) [6] integrate global context features with low- and high-level features. Wu *et al.* (CPD) [59] propose a framework for fast and accurate salient object detection named Cascaded Partial Decoder. Pang *et al.* (MINet) [41] propose the aggregate interaction modules and self-interaction modules to integrate the features from adjacent levels and obtain more efficient multi-scale features

from the integrated features. Chen *et al.* (RASNet) [5] employ residual learning to refine saliency maps progressively and design a novel top-down reverse attention block to guide the residual learning. Qin *et al.* (U^2 -Net) [45] propose Residual U-blocks (RSU) to capture more contextual information from different scales and increase the depth of the whole architecture without significantly increasing the computational cost. Xie *et al.* (PGNet) [61] integrates the features extracted by the Transformer and CNN backbones, enabling the network to combine the detection ability of Transformer with the detailed representation ability of CNN.

Utilizing auxiliary supervision: Many auxiliary maps such as edge maps, body maps and detail maps have been introduced to assist in predicting the saliency map for SOD in recent years. Liu *et al.* (PoolNet) [29] fuses edge information with saliency predictions in a multi-task training manner. Zhao *et al.* (EGNet) [72] perform interactive fusion after explicit modeling of salient objects and edges to jointly optimize the tasks of salient object detection and edge detection under the belief that these two tasks are complementary. Qin *et al.* (BASNet) [46] propose a hybrid loss which can focus on the pixel-level, patch-level, and map-level salient parts of the image. Su *et al.* (BANet) [51] use the selective features of boundaries to slight appearance change to distinguish salient objects and background. Feng *et al.* (AFNet) [14] design the Attentive Feedback Modules

(AFMs) and a Boundary-Enhanced Loss (BEL) to better explore the structure of objects and learn exquisite boundaries respectively. Wu *et al.* (SCRN) [60] propose a stacking Cross Refinement Unit (CRU) to simultaneously refine multi-level features of salient object detection and edge detection. Wei *et al.* (LDF) [58] explicitly decompose the original saliency map into body map and detail map so that edge pixels and region pixels have a more balanced distribution. Ke *et al.* (RCSB) [19] propose a contour-saliency blending module to exchange information between contour and saliency. Zhou *et al.* (ITSD) [74] propose an interactive two-stream decoder to explore multiple cues, including saliency, contour and their correlation. Qin *et al.* (IS-Net) [44] propose a simple intermediate supervision baseline using both feature-level and mask-level guidance for model training.

3. Proposed Method

First, we introduce our proposed Divide-and-Conquer Network and then describe the details of the two-level Residual nested-ASPP modules. Next we describe the Parallel Acceleration for DC-Net in detail. The training loss is described at the end of this section.

3.1. Divide-and-Conquer Network

The original use of the Divide-and-Conquer concept was to govern a nation, religion or country by first dividing it and then controlling and ruling it. Later, the same concept was applied to algorithms. The idea behind it is quite simple: divide a large or complex problem into smaller, simpler problems. Once the solutions to these smaller problems are obtained, they can be combined to solve the original problem.

In this work, we propose a novel end-to-end network, named Divide-and-Conquer Network (DC-Net), by incorporating the concept of Divide-and-Conquer into the training process of salient object detection (SOD) networks. DC-Net divides the task of predicting saliency maps into n subtasks, each responsible for predicting different semantic information of saliency maps. To achieve this, we supervise each stage of the encoder of every subtask with distinct auxiliary maps, while using the same encoder for each subtask. To reduce the GPU memory cost, we add an input convolutional layer with a kernel size of 3×3 and a stride of 2 before the first stage of every subtask.

Here, we set n to 2 to build our DC-Net as shown in Fig. 3. DC-Net has 2 encoders **Encoder1** and **Encoder2**, each consisting of 4 stages (**En1_1**, **En2_1**, **En3_1**, **En4_1** and **En1_2**, **En2_2**, **En3_2**, **En4_2**), and a decoder consisting of 5 stages (**De1**, **De2**, **De3**, **De4**, **De5**). The input to each decoder stage (**De(N)**) is the concatenation of the output of **En(N)_1**, **En(N)_2**, and **De(N+1)**, where N is in $\{1, 2, 3, 4\}$, and the input to **De5** is the concatenation of the output

of **En4_1** and **En4_2** after downsampling. Our method generates all side output predicted maps **Sup1_1**, **Sup2_1**, **Sup3_1**, **Sup4_1**, **Sup1_2**, **Sup2_2**, **Sup3_2**, **Sup4_2**, **Sup1**, **Sup2**, **Sup3**, **Sup4**, and **Sup5** from all encoder and decoder stages similar to HED [62] by passing their outputs through a 3×3 convolutional layer and a sigmoid function, and then upsampling the logits of these maps to the input image size. We choose edge maps with width 4 (only for the pixels salient in the saliency maps) and location maps, as shown in Fig. 2 (i) and (c), as target maps for two subtasks, which learn edge and location representations of salient objects respectively. The saliency map is used to supervise each decoder stage. We choose the output predicted map **Sup1** as our final saliency map.

3.2. Two-Level Residual Nested-ASPP Modules

For tasks such as salient object detection or other pixel-level tasks, both local and global semantic information are crucial. Local semantic information can be learned by shallow layers of the network, while global information depends on the size of the receptive field of the network. The most typical methods of enlarging the receptive field are as follows. The first one is to use the atrous convolution proposed by Deeplab [3]. The atrous convolution can obtain a larger receptive field than ordinary convolution without sacrificing image resolution. The atrous spatial pyramid pooling (ASPP) (as shown in Fig. 4 (a)) consisting of atrous convolutions with different dilation rates obtains output feature maps with rich semantic information by fusing multi-scale features. The second is to use global average pooling (GAP) of different sizes similar to the pyramid pooling modules (PPM) (as shown in Fig. 4 (b)) proposed by PSPNet [71] to obtain prior information of different scales and different sub-regions, and then concatenate them with the original feature map, and after another convolutional layer, the output feature map with global semantic information is obtained. RSU[45] and RSFPN (which we modify based on RSU) is to continuously obtain feature maps of different scales through downsampling, then upsample and aggregate low-level and high-level with different scales step by step like U-Net [47] and FPN [28] (as shown in Fig. 4 (c)). Their shortcomings are also obvious. ASPP has the disadvantage of sparse pixel sampling. PPM requires the original feature map to have a good feature representation. U-Net and FPN sacrifice the high resolution of the feature map in the process of downsampling and require more convolutional layers to obtain a larger receptive field, which leads to a large model size.

Inspired by the methods mentioned above, we propose a novel two-level Residual nested-ASPP module, **ResASPP²**, to capture compact multi-scale features. In theory, **ResASPP²** can be extended to **ResASPPⁿ**, where the exponent n can be set as an arbitrary positive integer. We

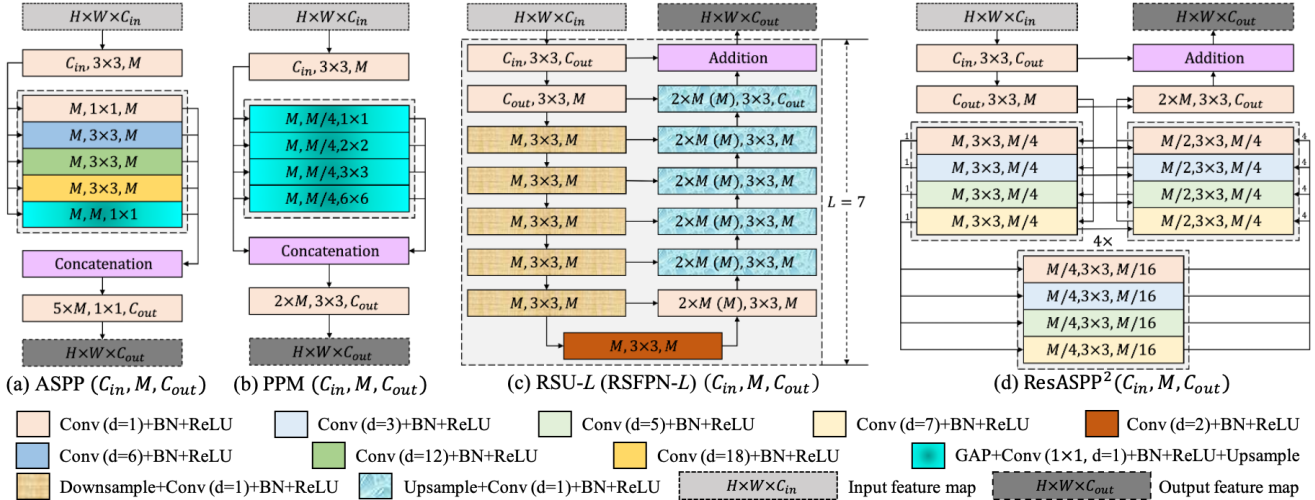


Figure 4. Illustration of existing multi-scale feature fusion module and our proposed two-level Residual nested-ASPP module: (a) ASPP-like module, (b) PPM-like module, (c) RSU module and its extension RSFPN module, where L is the number of layers in the encoder, (d) Our two-level Residual nested-ASPP module ResASPP².

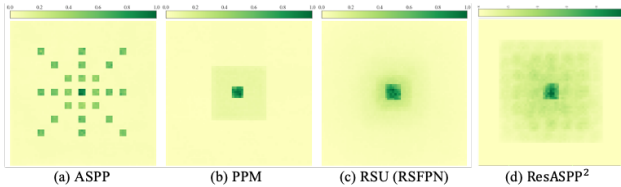


Figure 5. Comparison of the effective receptive field (ERF) of ASPP-like module, PPM-like module, RSU (RSFPN) module and our ResASPP² module.

set n to 2 as it balances performance and efficiency mostly. The structure of ResASPP²(C_{in} , M , C_{out}) is shown in Fig. 4 (d), where C_{in} , C_{out} denote input and output channels and M denotes the number of channels in the internal layers of ResASPP². Our ResASPP² mainly consists of three components:

- 1) an input convolution layer, which transforms the input feature map $\times (H \times W \times C_{in})$ to an intermediate map $\mathcal{F}(x)$ with channel of C_{out} which contains local feature.
- 2) Different from the dilation rate setting $\{1, 6, 12, 18\}$ in ASPP, we set the dilation rate of each layer of ResASPP² to $\{1, 3, 5, 7\}$ to obtain more compact pixel sampling. After two-level nested-ASPP, a feature map $ASPP^2(\mathcal{F}(x))$ with channel of C_{out} is obtained, which has a larger receptive field and more multi-scale contextual information than ASPP, under a smaller dilation rate. $ASPP^2$ represents the part of Fig. 4 (d) other than the input convolutional layer.

Fig. 5 presents a comparison of the effective receptive field (ERF) [35] of various modules, including a single ASPP-like module, PPM-like module, RSU

(RSFPN) module, and our proposed ResASPP² module. ResASPP² module outperforms other modules with the largest ERF and more compact ERF than ASPP. While RSU (RSFPN) module achieves its largest receptive field on the feature map with the lowest resolution after continuous downsampling, the decay of the gradient signal is exponential, resulting in a smaller ERF of its feature map obtained from the last layer after continuous upsampling and convolution. According to [9], the ERF is proportional to $\mathcal{O}(K\sqrt{L})$, where K is the kernel size and L is the depth (i.e., number of layers). Due to the fewer layers of ResASPP², the decay of the receptive field is negligible. Although RSU (RSFPN) has a larger largest receptive field than ResASPP², the ERF of its feature map obtained from the last layer is smaller than that of ResASPP². Furthermore, ResASPP² maintains high resolution of the feature maps all the time, while RSU (RSFPN) loses detail information in the process of continuous downsampling.

- 3) a residual connection is used to fuse local features with multi-scale features through addition: $\mathcal{F}(x) + ASPP^2(\mathcal{F}(x))$.

3.3. Parallel Acceleration

One advantage of the Divide-and-Conquer approach is its potential for parallel computing, which can improve the efficiency of the network. As shown in Fig. 6, the two identical encoders responsible for different subtasks can perform forward propagation simultaneously. To fully exploit this potential, we merge these two encoders into a single encoder with the same structure (**Parallel Encoder**) by reparameterizing operations such as convolutional lay-

ers, linear layers, matrix dot products, and layer normalization. Additionally, our ResASPP² module is accelerated by a proposed operation called **Merged Convolution**, which merges parallel convolutions with the same kernel size and output size. This allows for the computation of multiple parallel convolutions in a single step, reducing the total number of operations and accelerating the processing speed.

3.4. Loss Function

Our training loss function is defined as follows:

$$L = \sum_{e=1}^E (w_1^{(e)} l_1^{(e)} + w_2^{(e)} l_2^{(e)}) + \sum_{d=1}^D w^{(d)} l^{(d)} \quad (1)$$

In this equation, $l_1^{(e)}$ and $l_2^{(e)}$ are the losses of the side output auxiliary maps of **En(e)_1** and **En(e)_2** (referred to as **Sup(e)_1** and **Sup(e)_2** in Fig. 3), where e denotes the e_{th} encoder out of a total of E stages. $l^{(d)}$ is the loss of the side output saliency maps of **De(d)**, where d denotes the d_{th} decoder out of a total of D stages. The weights of each loss term are denoted by $w_1^{(e)}$, $w_2^{(e)}$, and $w^{(d)}$, respectively.

For each term l_1 and l_2 , we use the standard binary cross entropy to calculate the loss:

$$l_{bce} = - \sum_{(x,y)}^{(H,W)} [g(x,y) \log(p(x,y)) + (1 - g(x,y)) \log(1 - p(x,y))] \quad (2)$$

where (x,y) is the pixel coordinates and (H,W) is the height and width of the image. $g(x,y)$ and $p(x,y)$ denote the pixel values of the ground truth and predicted probability map respectively. For each term l , to take the global structure of the image into account, in addition to using the standard binary cross entropy, we also use IoU to calculate the loss:

$$l_{iou} = 1 - \frac{\sum_{(x,y)}^{(H,W)} [g(x,y)p(x,y)]}{\sum_{(x,y)}^{(H,W)} [g(x,y) + p(x,y) - g(x,y)p(x,y)]} \quad (3)$$

where the notations are the same as Eq. 2. The goal of our training process is to minimize the overall loss L .

4. Experiments

4.1. Implementation Details

In the training process, we use data augmentation including horizontal flip, random crop, and multi-scale input images. Two pretrained ResNet-34 [15] and Swin-B [33] are used as the encoders of our DC-Net-R and DC-Net-S respectively, and other parameters are randomly initialized. The loss weights w_1^e , w_2^e and w^d are all set to 1. Stochastic gradient descent (SGD) optimizer with momentum [48]

is used to train our network and its learning rate is set to 0.01 for LR datasets (ResNet-34), 0.001 for HR datasets (ResNet-34), and 0.001 for LR datasets (Swin-B), other hyperparameters including momentum and weight decay are set to 0.9 and 0.0001. We set the batch size to 32 for LR datasets (ResNet-34), 4 for HR datasets (ResNet-34), and 8 for LR datasets (Swin-B) and train the network for around 60k iterations until the loss converges. In addition, we use apex¹ and fp16 to accelerate the training process. During inference, each image is first resized to 352×352 for LR datasets (ResNet-34), 1024×1024 for HR datasets (ResNet-34), and 384×384 for LR datasets (Swin-B). Our network is implemented based on PyTorch [42]. Both training and testing and other experiments are conducted on a single RTX 6000 GPU (24GB memory).

4.2. Parallel Acceleration Details

We directly implement the Merged Convolution with PyTorch without modifying the underlying code written in C language. Using the Merged Convolution and Parallel Encoder for training can result in large memory costs and low efficiency, therefore, we use Training-DC-Net and Inference-DC-Net in training and inference phase respectively. The Training-DC-Net does not merge any operation, and the Inference-DC-Net uses Merged Convolution and Parallel Encoder. The parameters are copied from Training-DC-Net to Inference-DC-Net based on specific rules before inference.

4.3. Evaluation Metrics

To provide relatively comprehensive and unbiased evaluation of the quality of those output probability maps against the ground truth, nine different metrics including (1) Precision-Recall (PR) curves, (2) F-measure curves, (3) maximal F-measure ($max F_\beta \uparrow$) [1], (4) Mean Absolute Error ($MAE \downarrow$), (5) weighted F-measure ($F_\beta^w \uparrow$) [38], (6) structural measure ($S_\alpha \uparrow$) [10], (7) mean enhanced alignment measure ($E_\phi^m \uparrow$) [11], (8) relax human correction efforts (HCE_γ) [44], (9) mean boundary accuracy (mBA) [7] are used:

(1) **PR Curve** is generated using a collection of precision-recall pairs. When given a saliency probability map, its precision and recall scores are evaluated by comparing its thresholded binary mask with the actual ground truth mask. The precision and recall scores for the entire dataset are obtained by averaging the scores of individual saliency maps. By varying the thresholds between 0 and 255, a group of average precision-recall pairs for the dataset can be obtained.

(2) **F-measure Curve** draws the change of F-measure under different thresholds. For different thresholds be-

¹<https://github.com/NVIDIA/apex>

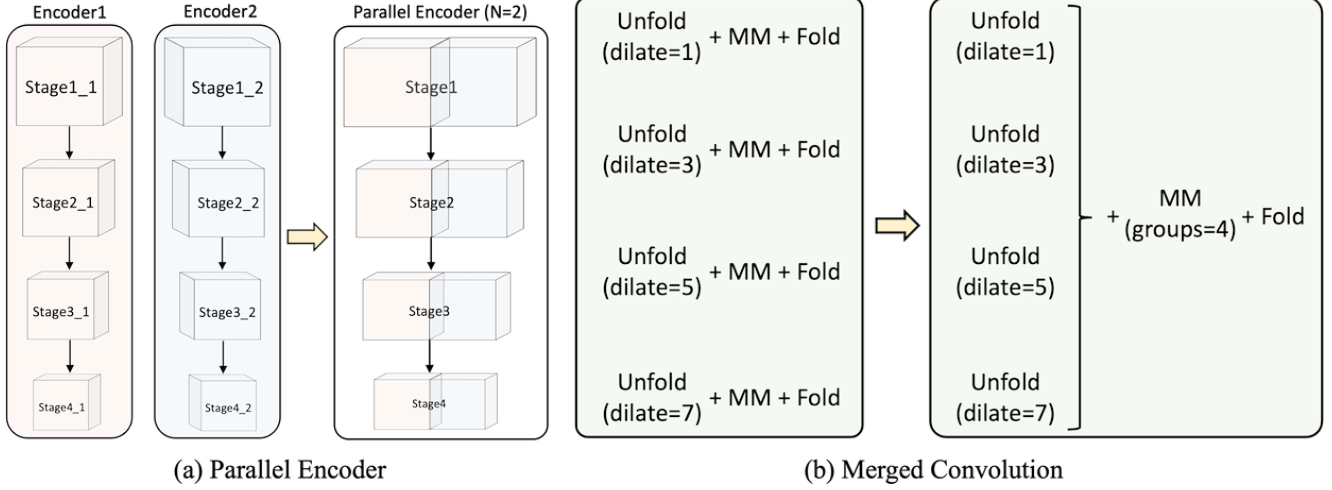


Figure 6. Illustration of the parallel encoder and merged convolution. ‘MM’ means Matrix Multiplication. A convolution operation can be separated as three parts: an unfold operation, a matrix multiplication, and a fold operation.

tween 0 and 255, the F-measure value of each dataset is obtained by averaging the F-measure value computed by comparing thresholded binary mask of each saliency probability map and its corresponding ground truth mask.

- (3) **F-measure** (F_β) is a weighted harmonic mean of precision and recall:

$$F_\beta = \frac{(1 + \beta^2) \times Precision \times Recall}{\beta^2 \times Precision + Recall} \quad (4)$$

We set the β^2 to 0.3 similar to previous works [1, 45]. F_β has different values for different thresholds between 0 and 255, and we report the maximum F_β ($maxF_\beta$) for each dataset.

- (4) **MAE** is the Mean Absolute Error which is calculated by averaging pixel-wise difference between the predicted saliency map (P) and the ground truth mask (G):

$$MAE = \frac{1}{H \times W} \sum_{x=1}^H \sum_{y=1}^W |P(x, y) - G(x, y)| \quad (5)$$

- (5) **weighted F-measure** (F_β^w) is proposed to overcome the possible unfair comparison caused by interpolation flaw, dependency flaw and equal-importance flaw [30]:

$$F_\beta^w = \frac{(1 + \beta^2) \times Precision^w \times Recall^w}{\beta^2 \times Precision^w + Recall^w} \quad (6)$$

We set β^2 to 1.0 as suggested in [2], and the weights (w) is different to each pixel according to its specific location and neighborhood information.

- (6) **S-measure** (S_α) is used to evaluate the object-aware (S_o) and region-aware (S_r) structural similarity, which is computed as:

$$S_\alpha = (1 - m)S_r + mS_o \quad (7)$$

We set α to 0.5 as suggested in [10].

- (7) **E-measure** (E_ϕ^m) considers the local pixel values with the image-level mean value in one term, which can be defined as:

$$E_\phi = \frac{1}{H \times W} \sum_{x=1}^H \sum_{y=1}^W \phi(x, y) \quad (8)$$

, where $\phi = f(\xi)$ is defined as the enhanced alignment matrix, ξ is defined as an alignment matrix, and $f(x) = \frac{1}{4}(1 + x)^2$ is a simple and effective function. We report mean E-measure (E_ϕ^m) for each dataset.

- (8) **relax HCE** (HCE_γ) aims to estimate the amount of human efforts needed to correct erroneous predictions and meet specific accuracy standards in practical scenarios, which can be defined as:

$$HCE_\gamma = compute_HCE(FN', FP', TP, epsilon) \quad (9)$$

We set γ to 5 and $epsilon$ to 2.0 as suggested in [44].

- (9) **mBA** is used to evaluate the boundary quality, and [20] shows that mBA itself cannot measure the performance of saliency detection, rather it only measures the quality of boundary itself.

4.4. Ablation Study

Ablation on Auxiliary Maps: In the auxiliary maps ablation, the goal is to find the most effective auxiliary map combination of subtasks. As shown in Table 1, we take the case of no subtask as the baseline, and we find that the performance of DC-Net-R is worse when the auxiliary maps all are saliency maps. We believe that predicting the saliency map is a difficult task, and the subtask should be simple, which may be the reason for the poor performance. Using the body and detail maps proposed in [58] as auxiliary maps yields a performance comparable to the baseline. Multi-value maps are more challenging than binary maps, making them unsuitable as subtasks. If we assume that predicting the saliency map involves a two-step process, where the first step is predicting the background pixel value as 0 and the second step is predicting the foreground pixel value as 1, then predicting the location map containing the location information of salient objects completes the first step, which is a simple binary prediction subtask. The edge map is a commonly used auxiliary map, and we have observe that the width of the edge pixel can impact the performance of the network. Our hypothesis is that a moderate width of the edge pixel can help the network focus more on the edges and avoid introducing excessive non-edge information.

Table 1. Results of ablation study on auxiliary maps. The table compares the results when encoder1 and encoder2 are supervised by different auxiliary maps including saliency, body, detail, edge1, edge2, edge3, edge4, edge5 and location maps as shown in Fig. 2. **Cyan** means the auxiliary maps that our DC-Net adopts.

Auxiliary Map	Encoder1	Encoder2	DUTS-TE					HKU-IS				
			F_{β}^w	MAE	maxF $_{\beta}$	S_{α}	E_{ϕ}^m	F_{β}^w	MAE	maxF $_{\beta}$	S_{α}	E_{ϕ}^m
-	-	-	.838	.040	.891	.888	.917	.902	.028	.940	.921	.950
Saliency	Saliency		.829	.040	.887	.885	.915	.901	.029	.939	.921	.950
Body	Detail		.837	.038	.891	.888	.917	.902	.029	.940	.920	.949
Edge1	Location		.845	.037	.894	.891	.921	.905	.028	.941	.921	.951
Edge2	Location		.845	.036	.896	.893	.923	.905	.028	.941	.922	.952
Edge3	Location		.847	.036	.897	.893	.923	.905	.028	.942	.921	.951
Edge4	Location		.852	.035	.899	.896	.927	.909	.027	.942	.924	.954
Edge5	Location		.845	.036	.895	.892	.922	.905	.028	.941	.922	.951

Ablation on Modules: In the module ablation, the goal is to validate the effectiveness of our newly designed two-level Residual nested-ASPP module (ResASPP²). Specifically, we fix the encoder part and the combination of subtasks (Edge4+Location) and replace each stage of the decoder with other modules in Fig. 4, including ASPP-like modules, PPM-like modules, RSU modules, and RSFPN modules. The module parameters C_{in} , M , and C_{out} of each stage of different modules are the same.

Table 2 shows the model size, FPS, and performance on DUTS-TE, HKU-IS datasets of DC-Net using different modules. Compared with RSU and RSFPN, our ResASPP² has a smaller model size when the FPS is competitive with them, and achieves better results on the datasets. Compared with the traditional two multi-scale contextual modules ASPP-like module and PPM-like module, ResASPP²

greatly improves the performance on the datasets. Therefore, we believe that our newly designed ResASPP² can achieve better results than other modules in this salient object detection task.

Table 2. Results of ablation study on modules. The structure of ASPP-like module, PPM-like module, RSU module, RSFPN module and ResASPP² module are shown in Fig. 4. **Cyan** means the module that our DC-Net adopts to the decoder.

Module	Size (MB)	FPS	DUTS-TE					HKU-IS				
			F_{β}^w	MAE	maxF $_{\beta}$	S_{α}	E_{ϕ}^m	F_{β}^w	MAE	maxF $_{\beta}$	S_{α}	E_{ϕ}^m
ASPP [3]	269.3	66	.826	.040	.892	.878	.905	.893	.032	.938	.913	.939
PPM [71]	266.5	77	.830	.039	.885	.886	.915	.905	.028	.939	.922	.952
RSU [45]	425.3	61	.842	.038	.894	.892	.920	.906	.028	.941	.923	.952
RSFPN	374.1	63	.844	.038	.895	.894	.923	.906	.027	.942	.924	.952
ResASPP²	356.3	60	.852	.035	.899	.896	.927	.909	.027	.942	.924	.954

Ablation on Parallel Acceleration: As shown in Table 3, the ablation study on parallel acceleration compares the time costs of DC-Net-R with and without acceleration of encoder or ResASPP². Training-DC-Net and Inference-DC-Net have the lowest time costs in the training phase and inference phase, respectively. As we can see, the accelerated encoder and ResASPP² are 5 (21) ms and 9 (13) ms faster for DC-Net-R (DC-Net-S), respectively, for a total of 14 (34) ms faster.

Table 3. Results of ablation study on parallel acceleration. ✓ and ✗ denote with and without acceleration respectively. **Cyan** and **Magenta** denote Training-DC-Net and Inference-DC-Net respectively. The batch sizes of training phase here are 12 (DC-Net-R) and 4 (DC-Net-S).

Parallel Acceleration		DC-Net-R			DC-Net-S		
Encoder	ResASPP ²	Training time (ms)	Inference time (ms)	Max batch size	Training time (ms)	Inference time (ms)	Max batch size
✗	✗	430	31	47	553	69	8
✓	✗	2055	26	46	682	48	7
✗	✓	665	22	24	619	56	6
✓	✓	2314	17	24	756	35	5

Ablation on Fusion Ways and Number of Encoders: In the ablation study on auxiliary maps, we demonstrate that supervising the model with an inappropriate combination of auxiliary maps can lead to a decrease in model performance, while a reasonable combination can increase model performance. In this ablation study, our goal is to prove the following idea: more encoders more effective. Therefore, finding a reasonable combination of auxiliary maps for more encoders is necessary. Additionally, we compare the effects of two different feature fusion ways. Considering that models using concatenation for feature fusion will have more parameters and computational complexity compared to the addition-based fusion way, we conduct an ablation study on the number of encoders using the addition-based fusion way. As shown in Table 4, with an increase in the number of encoders, the model performance improves and the number of parameters also increases. Model efficiency remains relatively stable due to the utilization of our **Parallel Encoder**.

Table 4. Results of ablation study on fusion ways and number of encoders. ✓ and ✗ denote with and without auxiliary map combination Edge4+Location. 'A' denotes addition and 'C' denotes concatenation.

Fusion Way	Number of Encoders	Auxiliary Map	Size (MB)	FPS	DUTS-TE					HKU-IS				
					F_{β}^w	MAE	$maxF_{\beta}$	S_{α}	E_{ϕ}^m	F_{β}^w	MAE	$maxF_{\beta}$	S_{α}	E_{ϕ}^m
A	1	✗	132.3	62	.836	.040	.890	.888	.916	.902	.029	.939	.920	.950
A	2	✗	211.4	61	.838	.039	.892	.887	.917	.903	.029	.940	.921	.951
A	3	✗	296.5	59	.842	.038	.894	.891	.919	.906	.028	.941	.923	.952
A	4	✗	391.8	57	.846	.036	.896	.892	.923	.909	.027	.943	.924	.954
A	2	✓	211.4	61	.846	.036	.897	.893	.923	.905	.028	.940	.922	.952
C	2	✓	356.3	60	.852	.035	.899	.896	.927	.909	.027	.942	.924	.954

By comparing the results in the 2_{nd} row and the 5_{th} row, we once again demonstrate that supervising the model with a reasonable combination of auxiliary maps can enhance model performance. We find that using concatenation for feature fusion performs better than addition, when not considering model size, we choose concatenation as the feature fusion way for DC-Net.

4.5. Experiments on Low-Resolution Saliency Detection Datasets

4.5.1 Datasets

Training dataset: DUTS dataset [53] is the largest and most frequently used training dataset for salient object detection currently. DUTS can be separated as a training dataset **DUTS-TR** and **DUTS-TE**, and we train our network on **DUTS-TR**, which contains 10553 images in total.

Evaluation datasets: We evaluate our network on five frequently used benchmark datasets including: **DUTS-TE** [53] with 5019 images, **DUT-OMRON** [65] with 5168 images, **HKU-IS** [22] with 4447 images, **ECSSD** [63] with 1000 images, **PASCAL-S** [25] with 850 images. In addition, we also measure the model performance on the challenging **SOC** (Salient Object in Clutter) test dataset [12] to show the generalization performance of our network in different scenarios.

4.5.2 Comparison with State-of-the-arts

4.5.2.1 Dataset-Based Analysis

We compare our DC-Net-R with 18 recent four years state-of-the-art convolution-based methods including one **RSU** based model: **U²-Net**; one **ResNet-34** based model: **BAS-Net**; two **VGG-16** [50] based model: **AFNet**, **RASNet**; six **ResNet-50** based model: **SCRN**, **BANet**, **F³Net**, **GC-PANet**, **LDF**, **RCSB**; for the other eight methods **PoolNet**, **EGNet**, **CPD**, **MINet**, **CAGNet**, **GateNet**, **ITSD**, **ICON**, we selected their better models based on **ResNet** or **VGG** for comparison. We also compare our DC-Net-S with 3 state-of-the-art self-attention-based methods including one **T2T-ViT_t-14** based model: **VST**; one **Swin-B** based model: **ICON-S**; one **PVT** based model: **SelfReformer**. For a fair comparison, we use the salient object detection results provided by the authors, and the same inference code is used to

test the FPS of methods.

Quantitative Comparison: Table 5 compares five evaluation metrics including $maxF_{\beta}$, MAE , F_{β}^w , S_{α} and E_{ϕ}^m of our proposed method with others. As we can see, our DC-Net performs against the existing methods across almost all five traditional benchmark datasets in terms of nearly all evaluation metrics. Fig. 7 illustrates the precision-recall curves and F-measure curves which are consistent with Table 5. The two red lines belonging to the proposed method are higher than the other curves, which further shows the effectiveness of prior knowledge and large ERF.

Qualitative Comparison: Fig. 8 shows the sample results of our method and other eight best-performing methods and the method with the first best FPS in Table 5, which intuitively demonstrates the promising performance of our method in different scenarios.

The 1_{st} and 2_{nd} rows of Fig. 8 show the results for small and hidden objects. Among all methods, only our DC-Net can accurately find the location of the object in the 1_{st} row image and segment it. The 3_{rd}, 4_{th} and 5_{th} rows show the results for large objects that extend to the edges of the image and our method can accurately segment the salient objects with high confidence. The 6_{th}, 7_{th} and 8_{th} rows show the scenario where there are multiple objects of the same categories that are near or far. We can find that our DC-Net is able to segment all objects accurately, while other methods miss one or more objects. The 9_{th}, 10_{th} and 11_{th} rows represent the scenario of objects with thin structures. As we can observe, our DC-Net can accurately segment even better than the chair part of the ground truth of the 10_{th} row. The 11_{th} and 12_{th} rows show the scenario where the image has a complex background. In this case, most of the time it is difficult for humans to distinguish the foreground from the background accurately. Compared with other methods, our method shows a better performance.

Failure Cases: In comparing the ground truths (GTs) and Ours-Rs of the 1_{st} row of Fig. 9, we observe that our predicted saliency maps segment some objects in addition to the salient object in the GTs. However, these objects are crucial for providing contextual information, and we believe they possess similar saliency to the salient objects in the GTs. **In the process of dataset annotation, the pho-**

Table 5. Comparison of our method and 21 SOTA methods on DUTS-TE, DUT-OMRON, HKU-IS, ECSSD, and PASCAL-S in terms of F_β^w (\uparrow), MAE (\downarrow), $maxF_\beta$ (\uparrow), S_α (\uparrow) and E_ϕ^m (\uparrow). **Red, Green and Blue** indicate the best, second best, and third best performance. The superscript of each score is the corresponding ranking. ‘-’ means missing data.

Method	Backbone	Size (MB)	Input Size	FPS	DUTS-TE(5019)					DUT-OMRON(5168)					HKU-IS(4447)					ECSSD(1000)					PASCAL-S(850)				
					F_β^w	MAE	$maxF_\beta$	S_α	E_ϕ^m	F_β^w	MAE	$maxF_\beta$	S_α	E_ϕ^m	F_β^w	MAE	$maxF_\beta$	S_α	E_ϕ^m	F_β^w	MAE	$maxF_\beta$	S_α	E_ϕ^m	F_β^w	MAE	$maxF_\beta$	S_α	E_ϕ^m
Convolution-Based Methods																													
PoolNet-R ₁₉ [29]	ResNet-50	278.5	300×400	54	817 ¹⁰	0.37 ³	889 ⁵	887 ⁶	910 ⁹	725 ¹³	0.54 ⁴	805 ¹³	831 ¹³	848 ¹²	888 ⁹	0.30 ⁴	936 ⁵	919 ³	945 ⁷	904 ⁹	0.35 ⁴	949 ³	926 ⁴	945 ⁵	809 ⁷	0.65 ⁷	879 ⁴	865 ²	896 ⁵
SCRN ₁₉ [60]	ResNet-50	101.4	352×352	38	803 ¹⁴	0.40 ⁶	888 ⁶	885 ⁷	900 ¹³	720 ¹⁴	0.56 ⁶	811 ¹⁰	837 ⁸	848 ¹²	876 ¹³	0.34 ⁸	934 ⁷	916 ⁶	935 ¹²	900 ¹¹	0.37 ⁵	950 ²	927 ³	939 ¹⁰	807 ⁹	0.63 ⁵	877 ²	869 ⁴	892 ⁶
AFNet ₁₉ [14]	VGG-16	133.6	224×224	-	785 ¹⁷	0.46 ¹⁰	863 ¹⁴	867 ¹³	893 ¹⁷	717 ¹⁶	0.57 ⁷	797 ¹⁵	826 ¹⁴	846 ¹⁴	869 ¹⁵	0.36 ⁶	922 ¹³	905 ¹⁰	934 ¹³	886 ¹⁴	0.42 ⁷	935 ¹¹	913 ¹¹	935 ¹²	797 ¹¹	0.70 ¹⁰	863 ¹²	849 ¹²	883 ¹²
BASNet ₁₉ [46]	ResNet-34	348.5	256×256	88	803 ¹⁵	0.48 ¹¹	859 ¹⁵	866 ¹⁴	896 ¹⁶	751 ¹⁵	0.56 ⁸	805 ¹³	836 ⁹	865 ¹⁵	889 ⁸	0.32 ⁹	928 ¹⁰	909 ⁹	943 ⁹	904 ⁹	0.37 ⁵	942 ⁹	916 ¹⁰	943 ⁷	793 ¹⁴	0.76 ¹³	854 ¹⁵	838 ¹⁶	879 ¹⁵
BANet ₁₉ [51]	ResNet-50	203.2	400×300	-	811 ¹²	0.40 ⁶	872 ¹¹	879 ¹⁰	913 ⁷	736 ¹⁰	0.59 ⁹	803 ¹⁴	832 ¹²	870 ¹⁷	886 ¹¹	0.32 ⁶	931 ⁹	913 ⁸	946 ⁶	908 ⁸	0.35 ⁴	945 ⁵	924 ⁴	948 ³	802 ¹⁰	0.70 ¹⁰	864 ¹¹	852 ¹¹	891 ¹⁴
EGNet-R ₁₉ [72]	ResNet-50	447.1	352×352	53	816 ¹¹	0.39 ⁵	889 ⁵	887 ⁶	907 ¹³	738 ⁹	0.53 ³	815 ⁷	841 ⁴	857 ¹⁵	887 ¹⁰	0.31 ⁵	935 ⁵	918 ⁴	944 ⁸	903 ¹⁰	0.37 ⁵	947 ⁵	925 ⁴	943 ⁷	795 ¹²	0.74 ¹²	863 ¹⁰	852 ¹¹	881 ¹⁴
CPD-R ₁₉ [59]	ResNet-50	192.0	352×352	37	795 ¹⁴	0.43 ⁹	863 ¹³	869 ¹²	898 ¹⁴	719 ¹⁵	0.56 ⁸	797 ¹⁵	825 ¹⁵	847 ¹⁵	875 ¹⁴	0.34 ⁸	925 ¹²	905 ¹⁰	938 ¹⁰	898 ¹²	0.37 ⁵	939 ⁹	918 ⁸	942 ⁸	792 ¹⁵	0.71 ¹¹	859 ¹⁴	848 ¹³	882 ¹³
U ² -Net ₂₀ [45]	RSU	176.3	320×320	41	804 ¹⁴	0.45 ⁹	876 ¹⁰	874 ¹¹	897 ¹⁵	759 ¹³	0.54 ⁴	823 ³	847 ²	867 ¹³	889 ⁸	0.31 ⁵	935 ⁵	916 ⁶	949 ⁹	910 ⁷	0.33 ²	951 ¹	928 ³	947 ⁴	792 ¹⁵	0.74 ¹²	859 ¹⁴	844 ¹⁴	873 ¹⁶
RASNet ₂₀ [5]	VGG-16	98.6	352×352	83	827 ⁷	0.37 ³	886 ⁷	884 ⁸	920 ⁴	743 ⁸	0.55 ⁵	815 ⁷	836 ⁶	866 ¹⁶	894 ⁶	0.30 ⁴	933 ⁸	915 ⁷	950 ⁴	913 ⁸	0.34 ³	948 ⁴	925 ⁵	950 ²	-	-	-	-	-
F ³ Net ₂₀ [57]	ResNet-50	102.5	352×352	63	835 ⁵	0.35 ²	891 ⁴	888 ⁵	920 ⁴	747 ⁷	0.53 ³	813 ⁸	838 ⁷	864 ¹⁶	900 ⁴	0.28 ²	937 ⁴	917 ⁵	952 ³	912 ⁵	0.33 ²	945 ⁵	924 ⁴	948 ³	816 ⁴	0.61 ³	871 ⁶	861 ⁵	898 ⁴
MINet ₂₀ [41]	ResNet-50	650.0	320×320	42	825 ⁷	0.37 ³	884 ⁸	884 ⁸	917 ⁵	738 ⁹	0.56 ⁸	810 ¹¹	833 ¹¹	860 ¹⁷	897 ⁵	0.29 ³	935 ⁵	919 ³	952 ³	911 ⁶	0.33 ²	947 ⁵	925 ⁴	950 ²	808 ⁸	0.66 ⁸	860 ¹³	842 ¹⁵	893 ⁵
CAGNet-R ₂₀ [39]	ResNet-50	199.8	480×480	-	817 ¹⁰	0.40 ⁶	867 ¹²	864 ¹⁵	909 ¹⁰	729 ¹²	0.54 ⁴	791 ¹⁶	814 ¹⁶	855 ¹⁰	893 ⁷	0.30 ⁴	926 ¹¹	904 ¹¹	946 ⁶	903 ¹⁰	0.37 ⁵	937 ¹⁰	907 ¹²	941 ⁹	808 ⁸	0.66 ⁸	860 ¹³	842 ¹⁵	893 ⁵
GateNet-R ₂₀ [73]	ResNet-50	514.9	384×384	65	809 ¹³	0.40 ⁶	888 ⁶	885 ⁷	906 ¹²	729 ¹²	0.55 ⁵	818 ⁶	838 ⁷	855 ¹⁷	880 ¹²	0.33 ⁷	933 ⁸	915 ⁷	937 ¹¹	894 ¹³	0.40 ⁶	945 ⁵	920 ⁵	950 ²	809 ⁷	0.64 ⁵	866 ¹⁰	856 ¹⁰	896 ⁶
ITSD-R ₂₀ [74]	ResNet-50	106.2	288×288	52	824 ⁸	0.41 ⁷	883 ⁹	885 ⁷	913 ⁷	750 ⁶	0.51 ⁵	821 ⁴	840 ⁵	865 ¹¹	894 ⁶	0.31 ⁵	934 ⁷	917 ⁵	947 ⁵	910 ⁷	0.34 ³	947 ⁵	925 ⁴	947 ⁴	812 ⁶	0.66 ⁸	870 ⁷	859 ⁷	894 ⁷
GCANet ₂₀ [6]	ResNet-50	268.6	288×288	61	821 ⁹	0.38 ⁴	888 ⁶	891 ³	911 ⁸	734 ¹¹	0.56 ⁸	819 ⁷	839 ⁶	853 ¹¹	889 ⁸	0.31 ⁵	938 ³	920 ²	944 ⁸	903 ¹⁰	0.35 ⁴	948 ⁴	927 ³	944 ⁷	808 ⁸	0.62 ¹	869 ⁸	864 ³	895 ⁵
LDF ₂₀ [58]	ResNet-50	100.9	352×352	63	845 ²	0.34 ¹	897 ²	892 ²	925 ²	752 ⁴	0.52 ²	820 ⁵	839 ⁶	865 ⁵	904 ²	0.28 ²	939 ²	919 ³	953 ²	915 ³	0.34 ³	950 ²	924 ⁴	948 ³	822 ²	0.60 ²	874 ⁵	863 ⁴	903 ¹
ICON-R ₂₁ [75]	ResNet-50	132.8	352×352	53	837 ⁴	0.37 ³	892 ³	889 ⁴	924 ³	761 ²	0.57 ²	825 ²	844 ³	876 ⁴	902 ³	0.29 ³	939 ²	920 ²	953 ²	918 ⁴	0.32 ¹	950 ²	929 ⁴	954 ¹	818 ³	0.64 ⁵	876 ³	861 ⁵	899 ³
RCSB ₂₂ [19]	ResNet-50	107.4	256×256	21	840 ³	0.35 ²	889 ⁵	881 ⁹	919 ⁵	752 ⁴	0.49 ¹	809 ¹²	835 ¹⁰	858 ⁸	909 ¹	0.27 ¹	938 ³	919 ³	954 ¹	916 ²	0.34 ³	944 ⁷	922 ⁷	950 ²	826 ¹	0.69 ¹	875 ⁴	860 ⁶	902 ²
DC-Net-R (Ours-R)	ResNet-34	356.3	352×352	60	852 ¹	0.35 ²	899 ¹	896 ¹	927 ¹	772 ¹	0.53 ³	827 ¹	849 ¹	876 ¹	909 ¹	0.27 ¹	942 ¹	924 ¹	954 ¹	913 ⁴	0.34 ³	949 ¹	924 ⁴	945 ¹	814 ⁴	0.65 ⁶	874 ⁵	857 ⁹	892 ²
Self-Attention-Based Methods																													
VST ₂₁ [32]	T2T-ViT ₁₋₁₄	178.4	224×224	35	828 ⁴	0.37 ⁴	890 ⁴	896 ⁴	919 ⁴	755 ⁴	0.58 ⁸	824 ⁴	850 ⁴	871 ⁴	897 ⁴	0.29 ⁴	942 ⁴	928 ⁴	952 ⁴	910 ⁴	0.33 ³	951 ⁴	932 ⁴	951 ⁴	816 ³	0.61 ⁴	875 ⁴	872 ⁴	902 ⁴
ICON-S ₂₁ [75]	Swin-B	383.5	384×384	29	886 ²	0.25 ²	920 ²	917 ²	954 ¹	804 ²	0.43 ²	855 ²	869 ²	900 ¹	925 ²	0.22 ²	951 ²	935 ²	968 ¹	936 ²	0.23 ¹	961 ²	941 ²	966 ¹	854 ¹	0.48 ¹	896 ²	885 ²	924 ¹
SelfReformer ₂₂ [66]	PVT	366.7	224×224	21	872 ³	0.27 ³	916 ³	911 ³	943 ³	784 ³	0.43 ²	837 ³	861 ³	884 ³	913 ³	0.24 ³	947 ³	931 ³	960 ³	926 ³	0.27 ²	958 ³	936 ³	957 ³	848 ²	0.51 ³	894 ³	881 ³	919 ²
DC-Net-S (Ours-S)	Swin-B	1495.0	384×384	29	895 ¹	0.23 ¹	930 ¹	925 ¹	952 ¹	809 ¹	0.39 ¹	857 ¹	875 ¹	898 ²	929 ¹	0.21 ¹	956 ¹	941 ¹	966 ²	941 ¹	0.23 ¹	966 ¹	947 ¹	965 ²	854 ¹	0.49 ²	899 ¹	887 ¹	917 ³

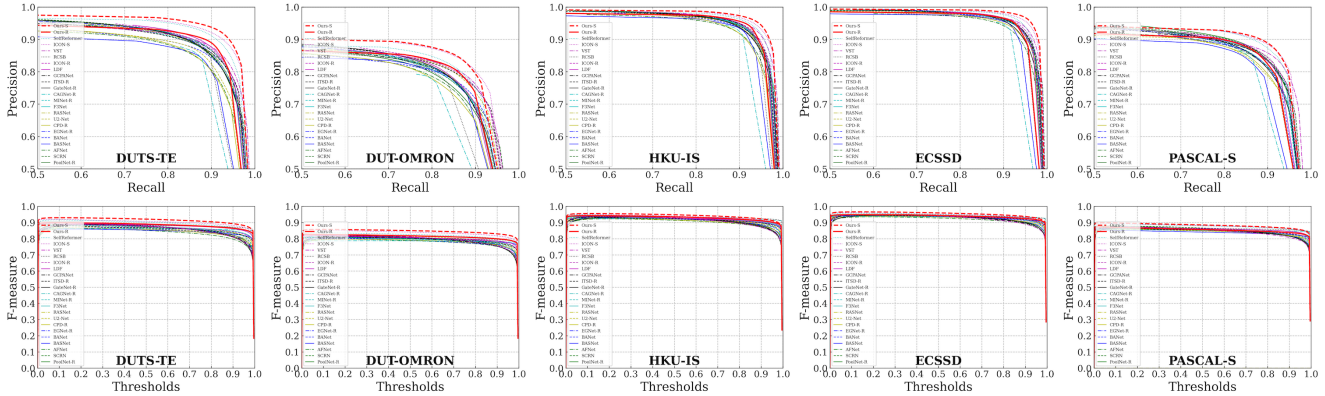


Figure 7. First row: Precision-Recall Curves comparison on five low-resolution saliency benchmark datasets. Second row: F-measure Curves comparison on five low-resolution saliency benchmark datasets.

topographer’s intention must be considered. For instance, the first example depicts a nail embedded in a tree trunk. In practical applications, segmenting only an overhead nail would destroy the image’s original semantic information. The third image shows a child playing on a slide in a park, with the slide being crucial in reserving the meaning of the image, while the park is relatively unimportant and should be considered as the background. One might ask, what if I only want to keep the portrait in the image for replacing the background in practical application? We call this task as portrait matting [49] and it has corresponding datasets for the demand. For salient object detection (SOD) task, the objective is to segment the most salient object in the image, or in other words, the object that attracts your attention the most when you first look at the image. In the 2nd row of Fig. 9, the salient objects in the GTs are completely opposite to the segmented objects in our predicted saliency maps. Our segmented objects are larger and have more distinct colors because larger and brighter objects tend to be more attention-grabbing. Moreover, we observe that in many datasets, for images that have both person and promi-

nent landscapes, annotators tend to annotate only the person and consider the landscapes as background, even though these landscapes are what the photographer aims to highlight.

4.5.2.2 Attribute-Based Analysis

In addition to the previous 5 most frequently used saliency detection datasets, we also evaluate our DC-Net on another challenging SOC test dataset [12]. The SOC dataset divides images into the following nine groups according to nine different attributes: AC (Appearance Change), BO (Big Object), CL (Clutter), HO (Heterogeneous Object), MB (Motion Blur), OC (Occlusion), OV (Out-of-View), SC (Shape Complexity), and SO (Small Object).

We compare our DC-Net with 18 state-of-the-art methods, including Amulet [69], DSS [16], NLDF [36], SRM [54], BMPM [68], C2SNet [24], DGRL [55], R³Net [8], RANet [4], AFNet [14], BASNet [46], CPD [59], EGNet [72], PoolNet [29], SCRNet [60], BANet [51], MINet [41] and PiCANet [30] in terms of attribute-based performance.

Quantitative Comparison: Table 6 compares five eval-

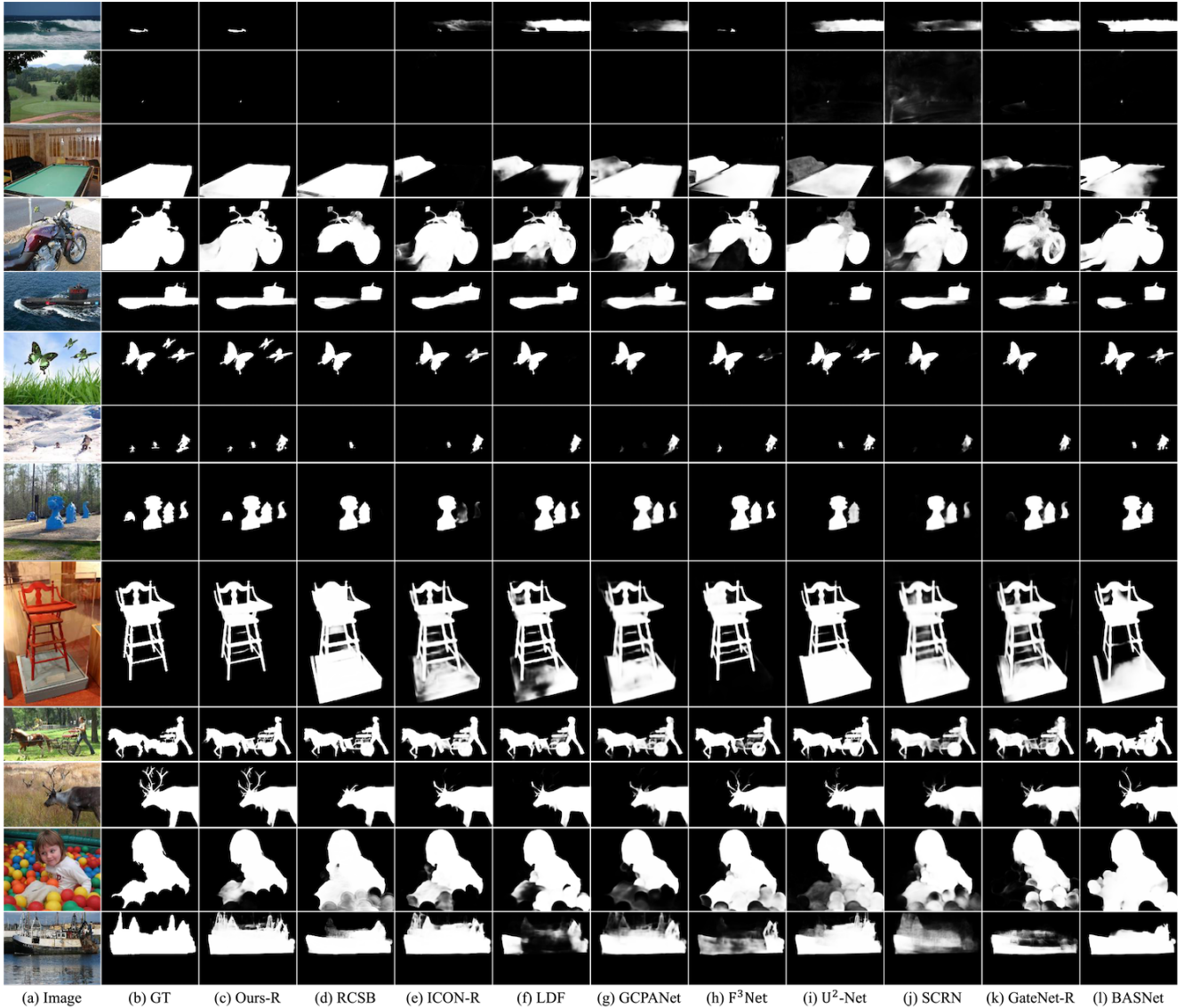


Figure 8. Low-resolution dataset-based qualitative comparison of the proposed method with nine other SOTA methods: (a) Image, (b) GT, (c) Ours-R, (d) RCSB, (e) ICON-R, (f) LDF, (g) GCPANet, (h) F^3 Net, (i) U^2 -Net, (j) SCRNet, (k) GateNet-R, (l) BASNet.

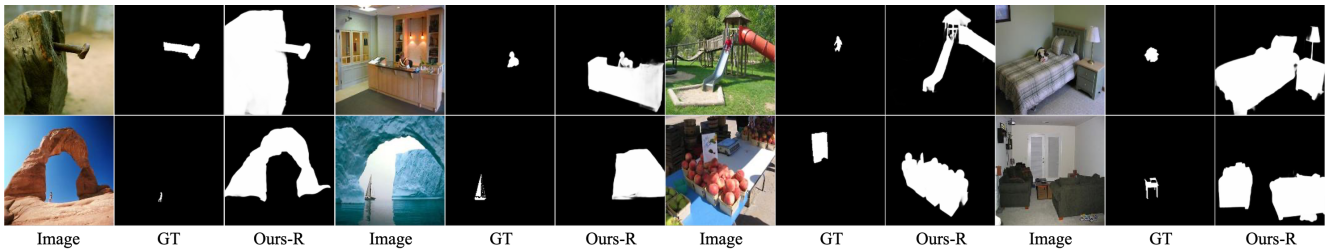


Figure 9. Failure cases of dataset-based analysis.

uation metrics including $\max F_\beta$, MAE , F_β^w , S_α and E_ϕ^m of our proposed method with others. As we can see, our DC-Net achieves the state-of-the-art performance on attributes AC, CL, OC, SC, SO and their average in terms

of almost all of the five evaluation metrics, and competitive performance on HO, MB and OV. On BO attribute, DC-Net performs relatively unremarkable and the cause of it is discussed in the failure cases part below. We calculate the

Table 6. Comparison of our method and 18 SOTA methods on SOC test dataset in terms of $maxF_\beta$ (\uparrow), MAE (\downarrow), F_β^w (\uparrow), S_α (\uparrow) and E_ϕ^m (\uparrow). **Red**, **Green** and **Blue** indicate the best, second best and third best performance. The superscript of each score is the corresponding ranking.

Attr	Metrics	Amulet	DSS	NLDF	SRM	BMPM	C2SNet	DGRL	R ³ Net	RANet	AFNet	BASNet	CPD	EGNet	PoolNet	SCRN	BANet	MINet	PiCANet	(Ours-R)
		[69]	[16]	[36]	[54]	[68]	[24]	[55]	[8]	[4]	[14]	[46]	[59]	[72]	[29]	[60]	[51]	[41]	[30]	
AC	$maxF_\beta$ \uparrow	.752 ¹⁴	.755 ¹³	.751 ¹⁵	.804 ⁷	.791 ¹⁰	.752 ¹⁴	.785 ¹¹	.756 ¹²	.745 ¹⁶	.801 ⁸	.804 ⁷	.811 ⁵	.822 ²	.801 ⁸	.817 ⁴	.819 ³	.808 ⁶	.795 ⁹	.834 ¹
	MAE \downarrow	.120 ¹⁶	.113 ¹⁴	.119 ¹⁵	.096 ¹¹	.098 ¹²	.109 ¹³	.081 ⁴	.135 ¹⁸	.132 ¹⁷	.084 ⁶	.083 ⁵	.089 ⁹	.085 ⁷	.093 ¹⁰	.078 ²	.086 ⁸	.079 ³	.093 ¹⁰	.076 ¹
	F_β^w \uparrow	.620 ¹⁶	.629 ¹⁵	.620 ¹⁶	.690 ¹¹	.680 ¹³	.647 ¹⁴	.718 ⁸	.593 ¹⁸	.603 ¹⁷	.712 ¹⁰	.727 ⁵	.721 ⁷	.731 ³	.713 ⁹	.723 ⁶	.739 ²	.730 ⁴	.681 ¹²	.768 ¹
	S_α \uparrow	.752 ¹³	.753 ¹²	.737 ¹⁴	.791 ⁹	.780 ¹⁰	.755 ¹¹	.791 ⁹	.713 ¹⁵	.709 ¹⁶	.796 ⁶	.799 ⁵	.799 ⁵	.806 ³	.795 ⁷	.809 ²	.806 ³	.802 ⁴	.793 ⁸	.824 ¹
	E_ϕ^m \uparrow	.790 ¹⁴	.787 ¹⁵	.783 ¹⁶	.824 ¹⁰	.815 ¹¹	.806 ¹³	.853 ⁴	.752 ¹⁸	.765 ¹⁷	.852 ⁵	.842 ⁹	.852 ⁵	.854 ³	.846 ⁷	.848 ⁶	.858 ²	.843 ⁸	.814 ¹²	.867 ¹
BO	$maxF_\beta$ \uparrow	.814 ¹⁶	.813 ¹⁷	.835 ¹²	.853 ¹¹	.826 ¹⁵	.863 ¹⁰	.888 ⁵	.782 ¹⁸	.725 ¹⁹	.874 ⁷	.868 ⁹	.895 ⁴	.829 ¹⁴	.831 ¹³	.921 ¹	.879 ⁶	.917 ³	.919 ²	.872 ⁸
	MAE \downarrow	.334 ¹²	.343 ¹⁵	.341 ¹⁴	.294 ¹¹	.292 ¹⁰	.257 ⁷	.207 ³	.432 ¹⁷	.440 ¹⁸	.236 ⁵	.247 ⁶	.236 ⁵	.358 ¹⁶	.339 ¹³	.217 ⁴	.261 ⁸	.175 ¹	.192 ²	.278 ⁹
	F_β^w \uparrow	.625 ¹⁵	.628 ¹⁴	.635 ¹³	.679 ¹²	.683 ¹¹	.739 ⁸	.794 ³	.471 ¹⁷	.469 ¹⁸	.750 ⁶	.749 ⁷	.755 ⁵	.602 ¹⁶	.625 ¹⁵	.784 ⁴	.729 ⁹	.828 ¹	.805 ²	.699 ¹⁰
	S_α \uparrow	.589 ¹³	.577 ¹⁶	.583 ¹⁴	.628 ¹¹	.619 ¹²	.667 ⁷	.696 ⁴	.455 ¹⁸	.437 ¹⁹	.671 ⁶	.660 ⁸	.679 ⁵	.546 ¹⁷	.578 ¹⁵	.707 ³	.657 ⁹	.743 ¹	.739 ²	.637 ¹⁰
	E_ϕ^m \uparrow	.566 ¹⁴	.554 ¹⁶	.556 ¹⁵	.630 ¹²	.635 ¹¹	.674 ⁸	.736 ³	.435 ¹⁸	.423 ¹⁹	.710 ⁵	.678 ⁷	.699 ⁶	.547 ¹⁷	.572 ¹³	.716 ⁴	.663 ⁹	.769 ¹	.750 ²	.641 ¹⁰
CL	$maxF_\beta$ \uparrow	.781 ¹¹	.731 ¹⁶	.727 ¹⁷	.770 ¹⁴	.771 ¹³	.748 ¹⁵	.785 ⁹	.687 ¹⁸	.681 ¹⁹	.803 ⁷	.792 ⁸	.806 ⁵	.782 ¹⁰	.779 ¹²	.811 ³	.808 ⁴	.822 ²	.805 ⁶	.830 ¹
	MAE \downarrow	.141 ¹⁰	.153 ¹²	.159 ¹³	.134 ⁸	.123 ⁷	.144 ¹¹	.119 ⁶	.182 ¹⁴	.188 ¹⁵	.119 ⁶	.114 ⁴	.112 ²	.139 ⁹	.134 ⁸	.113 ³	.117 ⁵	.108 ¹	.123 ⁷	.112 ²
	F_β^w \uparrow	.663 ¹³	.617 ¹⁵	.614 ¹⁶	.665 ¹²	.678 ¹⁰	.655 ¹⁴	.714 ⁶	.546 ¹⁷	.542 ¹⁸	.696 ⁷	.724 ³	.719 ⁴	.677 ¹¹	.681 ⁹	.717 ⁵	.725 ²	.719 ⁴	.691 ⁸	.746 ¹
	S_α \uparrow	.763 ¹⁰	.721 ¹⁵	.713 ¹⁶	.758 ¹²	.76 ¹¹	.742 ¹⁴	.769 ⁸	.659 ¹⁷	.633 ¹⁸	.767 ⁹	.773 ⁷	.786 ⁴	.757 ¹³	.760 ¹¹	.795 ²	.784 ⁵	.783 ⁶	.787 ³	.798 ¹
	E_ϕ^m \uparrow	.788 ¹²	.763 ¹⁴	.764 ¹³	.792 ¹⁰	.801 ⁷	.789 ¹¹	.824 ²	.789 ¹¹	.715 ¹⁵	.802 ⁶	.821 ⁴	.823 ³	.789 ¹¹	.800 ⁸	.815 ⁵	.824 ²	.819 ⁵	.793 ⁹	.834 ¹
HO	$maxF_\beta$ \uparrow	.804 ¹⁰	.789 ¹⁴	.778 ¹⁵	.800 ¹¹	.791 ¹³	.771 ¹⁶	.792 ¹²	.766 ¹⁷	.757 ¹⁸	.814 ⁹	.833 ⁴	.826 ⁷	.828 ⁶	.836 ³	.836 ³	.831 ⁵	.840 ¹	.819 ⁸	.838 ²
	MAE \downarrow	.119 ¹⁴	.124 ¹⁶	.126 ¹⁷	.115 ¹²	.116 ¹³	.123 ¹⁵	.104 ⁹	.135 ¹⁸	.143 ¹⁹	.102 ⁸	.097 ⁵	.098 ⁶	.106 ¹⁰	.100 ⁷	.096 ⁴	.094 ³	.089 ¹	.109 ¹¹	.092 ²
	F_β^w \uparrow	.688 ¹²	.660 ¹⁶	.661 ¹⁵	.696 ¹¹	.684 ¹³	.668 ¹⁴	.722 ⁸	.633 ¹⁷	.626 ¹⁸	.722 ⁸	.751 ⁴	.736 ⁷	.720 ⁹	.739 ⁶	.743 ⁵	.753 ³	.759 ²	.703 ¹⁰	.761 ¹
	S_α \uparrow	.790 ¹³	.767 ¹⁶	.755 ¹⁷	.794 ¹¹	.781 ¹⁴	.768 ¹⁵	.791 ¹²	.740 ¹⁸	.713 ¹⁹	.798 ¹⁰	.803 ⁸	.807 ⁷	.802 ⁹	.815 ⁵	.823 ¹	.819 ³	.821 ²	.809 ⁶	.818 ⁴
	E_ϕ^m \uparrow	.809 ¹³	.796 ¹⁶	.798 ¹⁵	.819 ¹⁰	.813 ¹²	.805 ¹⁴	.833 ⁸	.781 ¹⁷	.777 ¹⁸	.833 ⁸	.844 ⁵	.838 ⁷	.829 ⁹	.845 ⁴	.842 ⁶	.850 ³	.858 ¹	.817 ¹¹	.848 ³
MB	$maxF_\beta$ \uparrow	.680 ¹⁷	.717 ¹⁴	.698 ¹⁵	.746 ⁹	.741 ¹⁰	.692 ¹⁶	.739 ¹¹	.674 ¹⁸	.733 ¹³	.763 ⁷	.792 ²	.734 ¹²	.779 ⁵	.765 ⁶	.801 ¹	.783 ⁴	.783 ⁴	.750 ⁸	.790 ³
	MAE \downarrow	.142 ¹⁴	.132 ¹¹	.138 ¹²	.115 ⁸	.105 ³	.128 ¹⁰	.113 ⁷	.160 ¹⁵	.139 ¹³	.111 ⁶	.106 ⁴	.104 ²	.109 ⁵	.121 ⁹	.100 ¹	.104 ²	.105 ³	.100 ¹	.109 ⁵
	F_β^w \uparrow	.561 ¹⁵	.577 ¹³	.551 ¹⁶	.619 ¹¹	.651 ⁶	.593 ¹²	.655 ⁵	.489 ¹⁷	.576 ¹⁴	.626 ¹⁰	.679 ²	.655 ⁵	.649 ⁷	.642 ⁸	.690 ¹	.670 ⁴	.676 ³	.636 ⁹	.676 ³
	S_α \uparrow	.712 ¹⁴	.719 ¹³	.685 ¹⁶	.742 ¹¹	.762 ⁴	.719 ¹³	.744 ¹⁰	.657 ¹⁷	.696 ¹⁵	.734 ¹²	.754 ⁷	.753 ⁸	.762 ⁴	.751 ⁹	.792 ¹	.764 ³	.763 ³	.775 ²	.757 ⁶
	E_ϕ^m \uparrow	.738 ¹⁵	.753 ¹³	.739 ¹⁴	.777 ¹⁰	.812 ³	.777 ¹⁰	.823 ¹	.697 ¹⁶	.761 ¹²	.762 ¹¹	.803 ⁵	.809 ⁴	.789 ⁷	.779 ⁹	.816 ²	.803 ⁵	.793 ⁶	.812 ³	.787 ⁸
OC	$maxF_\beta$ \uparrow	.731 ¹³	.722 ¹⁵	.713 ¹⁶	.747 ¹¹	.747 ¹¹	.728 ¹⁴	.732 ¹²	.674 ¹⁸	.677 ¹⁷	.775 ⁵	.763 ⁹	.780 ²	.768 ⁷	.771 ⁶	.778 ³	.766 ⁸	.776 ⁴	.762 ¹⁰	.790 ¹
	MAE \downarrow	.143 ¹³	.144 ¹⁴	.149 ¹⁵	.129 ¹¹	.119 ⁹	.130 ¹²	.116 ⁷	.168 ¹⁶	.169 ¹⁷	.109 ³	.115 ⁶	.106 ²	.121 ¹⁰	.118 ⁸	.111 ⁴	.112 ⁵	.102 ¹	.119 ⁹	.102 ¹
	F_β^w \uparrow	.607 ¹⁴	.595 ¹⁵	.593 ¹⁶	.632 ¹²	.644 ¹⁰	.622 ¹³	.659 ⁸	.520 ¹⁸	.527 ¹⁷	.680 ³	.672 ⁷	.679 ⁶	.658 ⁹	.659 ⁸	.673 ⁶	.677 ⁵	.686 ²	.637 ¹¹	.708 ¹
	S_α \uparrow	.735 ¹⁴	.719 ¹⁵	.709 ¹⁶	.749 ¹¹	.752 ⁹	.738 ¹³	.747 ¹²	.653 ¹⁷	.641 ¹⁸	.771 ⁴	.750 ¹⁰	.773 ³	.754 ⁸	.756 ⁷	.775 ²	.766 ⁵	.771 ⁴	.765 ⁶	.787 ¹
	E_ϕ^m \uparrow	.762 ¹³	.760 ¹⁴	.755 ¹⁵	.780 ¹²	.799 ⁸	.784 ¹⁰	.808 ⁶	.705 ¹⁷	.718 ¹⁶	.819 ³	.810 ⁵	.818 ⁴	.798 ⁹	.800 ⁷	.800 ⁷	.808 ⁶	.821 ²	.783 ¹¹	.824 ¹
OV	$maxF_\beta$ \uparrow	.759 ¹⁵	.756 ¹⁶	.743 ¹⁷	.797 ¹²	.798 ¹¹	.768 ¹⁴	.808 ¹⁰	.696 ¹⁸	.689 ¹⁹	.818 ⁷	.819 ⁶	.816 ⁸	.810 ⁹	.796 ¹³	.826 ⁴	.835 ¹	.830 ²	.823 ⁵	.829 ³
	MAE \downarrow	.173 ¹³	.180 ¹⁴	.184 ¹⁵	.150 ¹¹	.136 ⁸	.159 ¹²	.125 ²	.216 ¹⁶	.217 ¹⁷	.129 ⁶	.134 ⁷	.125 ³	.146 ⁹	.148 ¹⁰	.126 ⁴	.119 ⁵	.117 ¹	.127 ⁵	.126 ⁴
	F_β^w \uparrow	.637 ¹³	.622 ¹⁴	.616 ¹⁵	.682 ¹¹	.701 ⁹	.671 ¹²	.733 ³	.527 ¹⁷	.529 ¹⁶	.723 ⁵	.721 ⁶	.724 ⁴	.707 ⁸	.697 ¹⁰	.723 ⁵	.751 ¹	.738 ²	.720 ⁷	.738 ²
	S_α \uparrow	.721 ¹⁵	.700 ¹⁶	.688 ¹⁷	.745 ¹³	.751 ¹⁰	.728 ¹⁴	.762 ⁷	.625 ¹⁸	.611 ¹⁹	.761 ⁸	.748 ¹¹	.765 ⁶	.752 ⁹	.747 ¹²	.774 ⁴	.779 ²	.775 ³	.781 ¹	.771 ⁵
	E_ϕ^m \uparrow	.750 ¹⁴	.737 ¹⁵	.736 ¹⁶	.778 ¹³	.806 ⁸	.789 ¹²	.828 ²	.663 ¹⁸	.664 ¹⁷	.816 ⁴	.803 ⁹	.809 ⁶	.802 ¹⁰	.795 ¹¹	.807 ⁷	.835 ¹	.822 ³	.809 ⁶	.814 ⁵
SC	$maxF_\beta$ \uparrow	.737 ¹²	.735 ¹⁴	.707 ¹⁷	.764 ¹⁰	.783 ⁸	.71 ¹⁶	.736 ¹³	.697 ¹⁸	.718 ¹⁵	.780 ⁹	.786 ⁷	.793 ⁴	.783 ⁸	.790 ⁵	.795 ³	.788 ⁶	.798 ²	.755 ¹¹	.816 ¹
	MAE \downarrow	.098 ¹²	.098 ¹²	.101 ¹⁴	.090 ¹⁰	.081 ⁷	.100 ¹³	.087 ⁹												

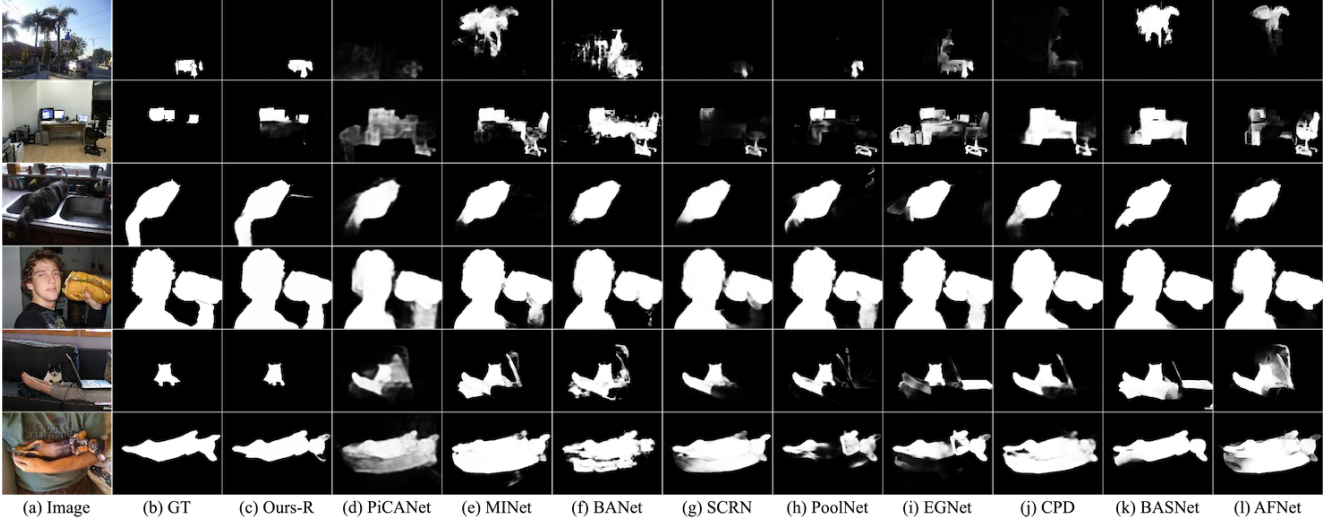


Figure 10. Low-resolution attribute-based qualitative comparison of the proposed method with nine other SOTA methods: (a) Image, (b) GT, (c) Ours-R, (d) PiCANet, (e) MINet, (f) BANet, (g) SCRNet, (h) PoolNet, (i) EGNNet, (j) CPD, (k) BASNet, (l) AFNet.



Figure 11. Failure cases of attribute-based analysis.

Table 8. Comparison of our method and 8 SOTA methods on DIS-TE, ThinObject5K, UHRSD, HRSOD, and DAVIS-S in terms of HCE_γ (\downarrow), mBA (\uparrow), MAE (\downarrow), F_β^w (\uparrow), and S_α (\uparrow). Red, Green and Blue indicate the best, second best, and third best performance. The superscript of each score is the corresponding ranking.

Method	Backbone	Size (MB)	Input Size	FPS	DIS-TE(2470)					ThinObject5K(5748)					UHRSD(5920)					HRSOD(2010)					DAVIS-S(92)				
					HCE_γ	mBA	MAE	F_β^w	S_α	HCE_γ	mBA	MAE	F_β^w	S_α	HCE_γ	mBA	MAE	F_β^w	S_α	HCE_γ	mBA	MAE	F_β^w	S_α	HCE_γ	mBA	MAE	F_β^w	S_α
SCRNet ₁₉ [60]	R-50	101.4	1024×1024	32	1344 ⁸	.703 ⁸	.076 ⁸	.685 ⁹	.818 ⁵	250 ⁸	.744 ⁹	.099 ¹	.743 ⁷	.818 ⁷	209 ⁷	.732 ⁸	.062 ⁴	.807 ⁷	.873 ⁴	247 ⁷	.694 ⁷	.068 ²	.757 ⁶	.855 ⁴	207 ⁸	.718 ⁹	.036 ³	.764 ⁶	.885 ²
CPN-Net ₁₉ [59]	R-50	192.0	1024×1024	28	1430 ⁹	.696 ⁹	.075 ⁷	.694 ⁷	.817 ⁶	253 ⁹	.752 ⁸	.090 ²	.761 ⁵	.826 ⁴	218 ⁸	.728 ⁷	.062 ⁴	.814 ⁸	.872 ⁵	262 ⁸	.694 ⁷	.074 ⁴	.746 ⁵	.839 ⁴	206 ⁷	.731 ⁸	.036 ³	.765 ⁶	.880 ⁴
F ³ Net ₂₀ [57]	R-50	102.5	1024×1024	58	1115 ⁵	.758 ²	.069 ³	.729 ⁴	.821 ³	188 ²	.800 ¹	.103 ⁸	.741 ⁸	.801 ⁸	173 ²	.764 ⁴	.067 ⁷	.804 ⁸	.855 ⁶	208 ²	.725 ²	.075 ⁵	.743 ⁶	.826 ³	160 ²	.759 ²	.040 ⁷	.738 ⁹	.852 ⁹
GCPANet ₂₀ [6]	R-50	268.6	1024×1024	60	1235 ⁵	.727 ⁶	.076 ⁸	.692 ⁸	.816 ⁷	212 ⁵	.781 ⁴	.093 ⁶	.757 ⁶	.825 ⁵	192 ⁵	.748 ⁵	.066 ⁶	.799 ⁹	.863 ⁶	231 ⁵	.704 ⁶	.084 ⁷	.711 ⁸	.818 ⁷	181 ⁵	.746 ⁵	.039 ⁶	.742 ⁷	.869 ⁷
LDF ₂₀ [58]	R-50	100.9	1024×1024	58	1159 ⁷	.751 ³	.070 ⁴	.730 ³	.820 ³	200 ³	.795 ³	.106 ⁷	.736 ⁹	.799 ⁹	180 ⁴	.761 ³	.064 ⁵	.810 ⁹	.860 ⁷	218 ⁴	.722 ⁴	.072 ³	.761 ³	.839 ⁴	173 ⁴	.755 ³	.038 ⁵	.747 ⁷	.860 ⁸
ICON-Net ₂₁ [75]	R-50	132.8	1024×1024	45	1337 ⁷	.711 ⁷	.072 ⁶	.715 ⁹	.809 ⁹	249 ⁷	.762 ⁷	.089 ⁴	.770 ⁴	.822 ⁶	221 ⁹	.723 ⁹	.069 ⁸	.808 ⁹	.856 ⁸	269 ⁹	.691 ⁸	.080 ⁵	.741 ⁷	.824 ⁵	206 ⁷	.737 ⁷	.035 ²	.767 ⁴	.876 ⁶
PGNet ₂₂ [61]	R-18+S-B	279.2	1024×1024	31	1285 ⁸	.728 ⁵	.056 ¹	.769 ⁴	.851 ¹	226 ⁶	.779 ⁵	.072 ⁵	.806 ³	.859 ¹	196 ⁶	.758 ⁶	.041 ¹	.872 ¹	.907 ¹	238 ⁶	.723 ³	.041 ¹	.844 ¹	.898 ¹	192 ⁶	.738 ⁶	.023 ¹	.848 ¹	.917 ¹
IS-Net ₂₂ [44]	RSU	176.6	1024×1024	39	1035 ²	.741 ⁴	.071 ⁵	.724 ²	.818 ²	202 ⁴	.776 ⁶	.085 ³	.778 ³	.831 ³	176 ³	.761 ²	.058 ³	.833 ³	.879 ³	211 ³	.712 ⁵	.072 ³	.757 ⁴	.839 ³	171 ³	.748 ⁴	.036 ⁴	.788 ³	.884 ³
DC-Net-R (Ours-R)	R-34	356.3	1024×1024	55	984 ¹	.765 ¹	.063 ²	.759 ²	.840 ²	180 ¹	.796 ²	.081 ²	.786 ²	.839 ²	163 ¹	.775 ¹	.053 ²	.844 ²	.885 ²	203 ¹	.728 ¹	.068 ²	.767 ²	.846 ²	159 ¹	.763 ¹	.037 ¹	.789 ²	.879 ²

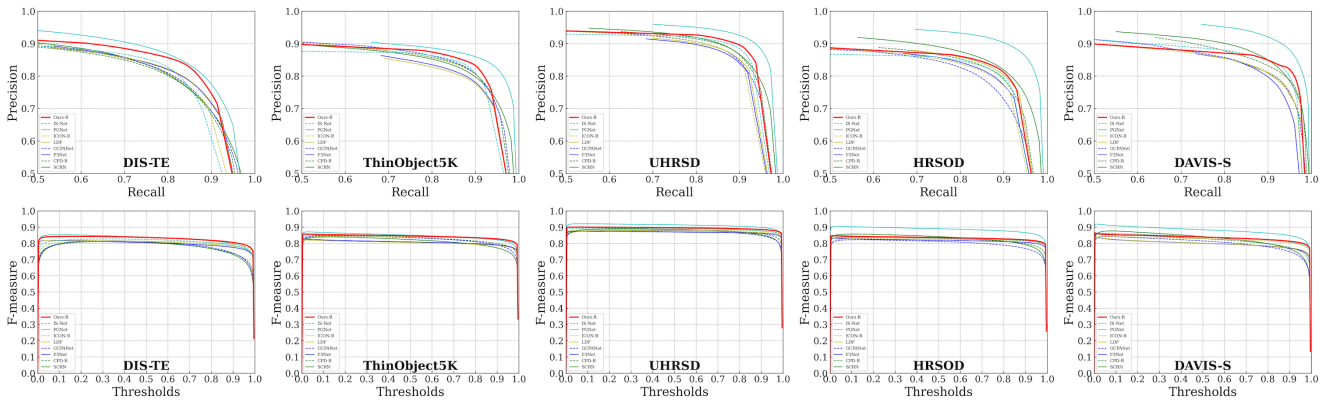


Figure 12. First row: Precision-Recall Curves comparison on five high-resolution saliency benchmark datasets. Second row: F-measure Curves comparison on five high-resolution saliency benchmark datasets.

sults of our method and other nine best-performing meth-

ods in Table 6, which intuitively demonstrates the promis-

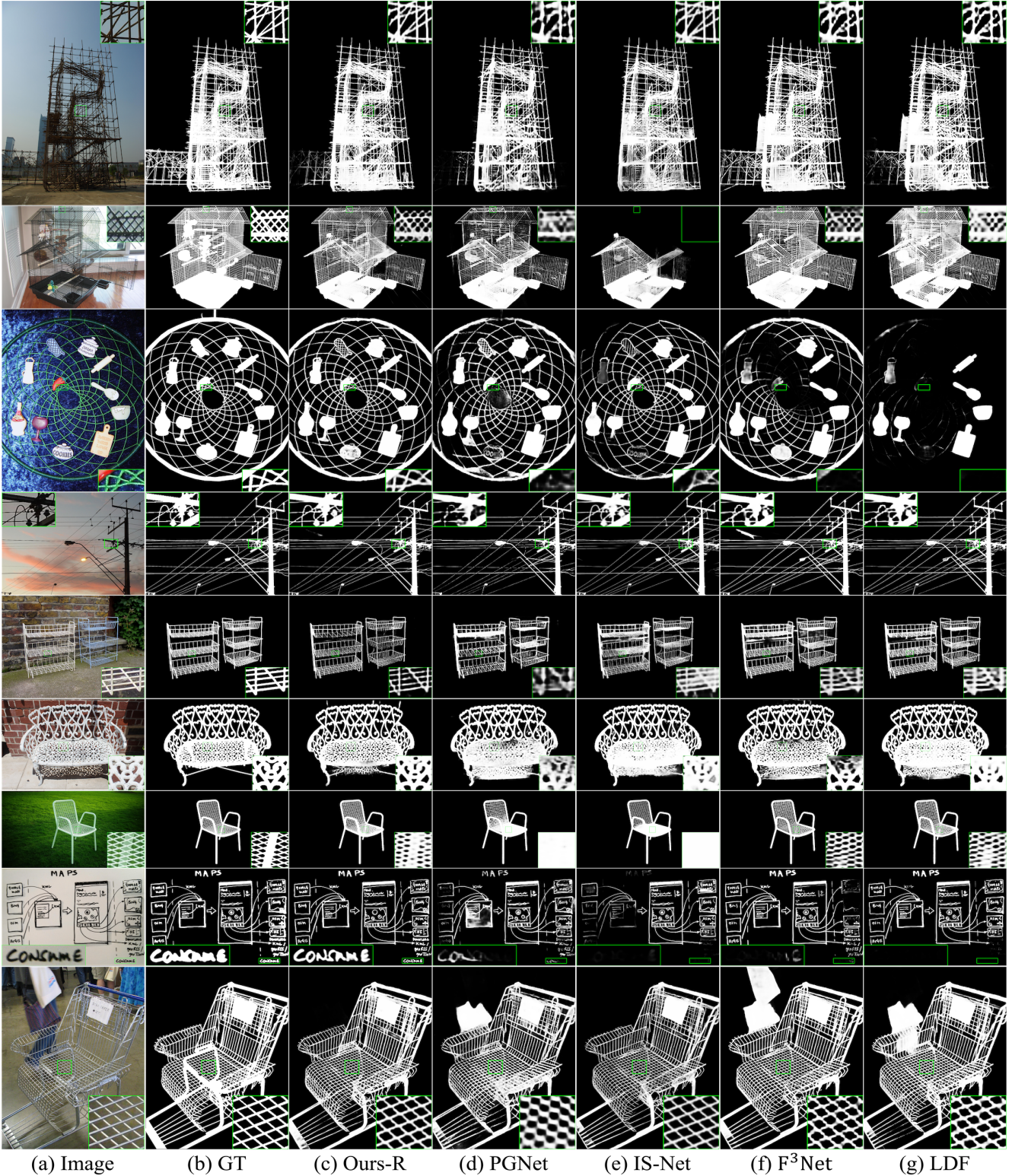


Figure 13. High-resolution qualitative comparison of the proposed method with four other SOTA methods: (a) Image, (b) GT, (c) Ours-R, (d) PGNet, (e) IS-Net, (f) F³Net, (g) LDF.

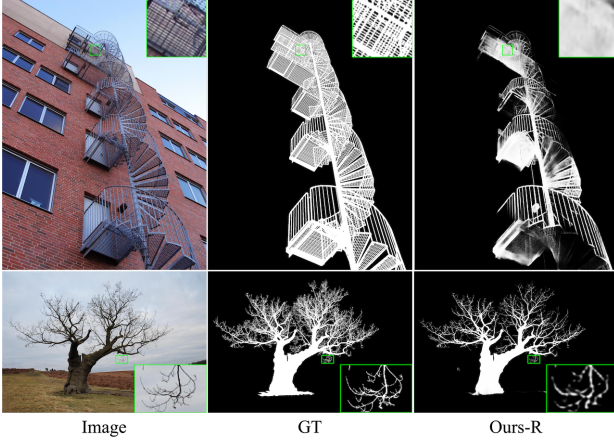


Figure 14. Failure cases of high-resolution images.

ing performance of our method in three scenarios different from those mentioned in dataset-based analysis.

The salient objects depicted in the 1st and 2nd rows of Fig. 10 possess relatively modest saliency scores when contrasted with other images, but still maintain higher saliency compared to other objects within the same image. This leads to a challenging task for models to accurately detect them. Our method is capable of accurately localizing such objects. The 3rd and 4th rows exhibit results for salient objects with low-contrast, such as the tail of the cat in the third row and the arm in the fourth row. Our DC-Net-R demonstrates robustness in accurately segmenting these objects from the background. In the 5th and 6th rows, salient objects are occluded by surrounding confusing objects. By discerning the photographer’s intent, it is apparent that the non-salient objects are not intended to draw attention in the image. Our method demonstrates accurate discrimination between salient and non-salient objects in such scenarios.

Failure Cases: In the dataset-based analysis, we show that DC-Net-R has a good ability to segment large single salient objects, while the performance of DC-Net on the BO attribute is relatively unremarkable. We find that the BO test dataset contains many images which have both large and small salient objects in different categories, such as people holding food and different kinds of food on the table shown in Fig. 11. Our findings suggest that our method is better suited for segmenting salient objects of the same category, rather than handling scenarios with multiple salient objects belonging to different categories.

4.6. Experiments on High-Resolution Saliency Detection Datasets

As the results of the methods proposed by researchers on low-resolution datasets gradually become saturated, the development of high-resolution and high-quality (HH) segmentation has become an inevitable trend, especially for the

meticulous fields of medical, aviation, and military. We suggest to use the following five datasets as training and evaluation datasets for HH methods: **DIS5K** [44], **ThinObject5K** [27], **UHRSD** [61], **HRSOD** [67] and **DAVIS-S** [43]. These datasets are all made for HH, Table 7 shows their data analysis, which is calculated following [44]. (H, W, D) and $(\sigma_H, \sigma_W, \sigma_D)$ represent the mean of the image height, width, and diagonal length and their standard deviations respectively. The object complexity of datasets is evaluated by three metrics including the *isoperimetric inequality quotient* ($IPQ \uparrow$) [40, 56, 64], the *number of object contours* ($C_{num} \uparrow$) and the *number of dominant points* ($P_{num} \uparrow$).

4.6.1 Datasets

Training dataset: **DIS5K** [44] can be separated as a training dataset **DIS-TR**, a validation dataset **DIS-VD** and four test datasets **DIS-TE1**, **DIS-TE2**, **DIS-TE3** and **DIS-TE4**. We choose **DIS-TR** as our training dataset (3000 images) because its object complexity is much higher than other datasets. We believe that when the model can accurately segment complex objects, it becomes easier to segment simple objects.

Evaluation datasets: We evaluate our network on five benchmark datasets including: **DIS-TE** with 2470 images consisting of **DIS-VD**, **DIS-TE1**, **DIS-TE2**, **DIS-TE3** and **DIS-TE4**, **ThinObject5K** [27] with 5748 images, **UHRSD** [61] with 5920 images, **HRSOD** [67] with 2010 images, **DAVIS-S** [43] with 92 images.

4.6.2 Comparison with State-of-the-arts

We compare our DC-Net with 8 state-of-the-art methods including one **RSU** based model: **IS-Net**; one **ResNet-18** and **Swin-B** based model: **PGNet**; six **ResNet-50** based model: **SCRN**, **F³Net**, **GCPANet**, **LDF**, **ICON-R**, **CPD-R**, we selected their better models based on **ResNet** or **VGG** for comparison. For a fair comparison, we run the official implementation of **IS-Net** which is trained on **DIS-TR** with pre-trained model parameters provided by the author to evaluate with the same evaluation code. Moreover, we re-train **PGNet**, **SCRN**, **F³Net**, **GCPANet**, **LDF**, **ICON-R**, and **CPD-R** on **DIS-TR** based on their official implementation provided by the authors. We choose the above methods since their source codes have great reproducibility. Among them, **IS-Net** and **PGNet** are designed for high resolution, and others are designed for low resolution.

Quantitative Comparison: Table 8 compares five evaluation metrics including HCE_γ , mBA , MAE , F_β^w , and S_α of our proposed method with others, where HCE_γ and mBA are designed for evaluating the detail quality of high-resolution saliency maps. As we can see, our DC-Net-R achieves state-of-the-art performance on almost all datasets

in terms of HCE_γ and mBA , and the second-best performance on DIS-TE, ThinObject5K, UHRSD, and HRSOD in terms of MAE , F_β^w , and S_α . We find that PGNet obtain SOTA results on all datasets in terms of MAE , F_β^w , and S_α and unremarkable results on HCE_γ and mBA , which indicate that Swin Transformer outperforms ResNet in detection but may not excel in capturing details. The Fig. 12 illustrates the precision-recall curves and F-measure curves which are consistent with the Table 8.

Qualitative Comparison: Fig. 13 shows the sample results of our method and the other four best-performing methods in Table 8, which intuitively demonstrates that our method can also achieve promising results on high-resolution datasets. Ours not only accurately detects salient objects but also produces smooth and high-confidence segmentation results for fine and dichotomous parts. In contrast, the segmentation results of PGNet, F³Net, and LDF appear rough. Although the detail quality of IS-Net is competitive, the confidence level is slightly lower. Specifically, the 3_{rd}, 8_{th}, and 9_{th} rows display large objects that almost occupy the entire image, while other methods either miss some parts or segment out incorrect parts. In contrast, our method can accurately segment them, demonstrating that the large and compact receptive field provided by *ResASPP*² enables the model with the ability to recognize holistic semantics.

Failure Cases: As shown in Fig. 14, both the Image and GT are displayed at the original pixel size, whereas the saliency map is obtained by downsampling the original image to 1024×1024 and then processing it through the model. As a result, a significant amount of precision and detail is lost, especially for extremely small parts. The spiral iron stair in 1_{st} row has densely staggered parts, resulting in a lot of holes of different sizes interspersed between the iron stairs. It is difficult for our method to segment such a dichotomous object with the input size of 1024×1024 . The branches in 2_{nd} row is a difficult case for highly accurate segmentation. It has the characteristics of irregular shape, uncertain direction, and meticulousity, which makes the confidence of predicted saliency maps low. Therefore, models that can handle higher-resolution input images to obtain detailed object structures, with acceptable memory usage, training and inference time costs on the mainstream GPUs are needed.

5. Conclusion

In this paper, we propose a novel salient object detection model DC-Net. Our DC-Net explicitly guides the model’s training process by using the concept of Divide-and-Conquer, and then obtains larger and more compact effective receptive fields (ERF) and richer multi-scale information through our newly designed two-level Residual nested-ASPP (*ResASPP*²) modules. Additionally, we hope

that our parallel version of ResNet and Swin-Transformer can promote the research of multiple encoder models. Experimental results on six public low-resolution and five high-resolution salient object detection datasets demonstrate that our DC-Net achieves competitive performance against 21 and 8 state-of-the-art methods respectively. We also demonstrate through experiments that edge maps with different edge widths have a significant impact on the model’s performance.

Although our model achieves competitive results compared to other state-of-the-art methods, the disadvantage of using multiple encoders leads to an increase in parameters. In the near future, we will explore different techniques such as distillation to address this issue. Furthermore, as mentioned above, how to find reasonable auxiliary map combinations for more encoders and how to enable the model to handle larger resolution input images in acceptable memory usage, training and inference time costs are also urgent issues to be addressed.

References

- [1] Radhakrishna Achanta, Sheila Hemami, Francisco Estrada, and Sabine Susstrunk. Frequency-tuned salient region detection. In *2009 IEEE conference on computer vision and pattern recognition*, pages 1597–1604. IEEE, 2009. 6, 7
- [2] Ali Borji, Ming-Ming Cheng, Huaizu Jiang, and Jia Li. Salient object detection: A benchmark. *IEEE transactions on image processing*, 24(12):5706–5722, 2015. 7
- [3] Liang-Chieh Chen, George Papandreou, Iasonas Kokkinos, Kevin Murphy, and Alan L Yuille. Deeplab: Semantic image segmentation with deep convolutional nets, atrous convolution, and fully connected crfs. *IEEE transactions on pattern analysis and machine intelligence*, 40(4):834–848, 2017. 2, 4, 8
- [4] Shuhan Chen, Xiuli Tan, Ben Wang, and Xuelong Hu. Reverse attention for salient object detection. In *Proceedings of the European conference on computer vision (ECCV)*, pages 234–250, 2018. 10, 12
- [5] Shuhan Chen, Xiuli Tan, Ben Wang, Huchuan Lu, Xuelong Hu, and Yun Fu. Reverse attention-based residual network for salient object detection. *IEEE Transactions on Image Processing*, 29:3763–3776, 2020. 3, 10
- [6] Zuyao Chen, Qianqian Xu, Runmin Cong, and Qingming Huang. Global context-aware progressive aggregation network for salient object detection. In *Proceedings of the AAAI conference on artificial intelligence*, volume 34, pages 10599–10606, 2020. 3, 10, 13
- [7] Ho Kei Cheng, Jihoon Chung, Yu-Wing Tai, and Chi-Keung Tang. Cascadepsp: Toward class-agnostic and very high-resolution segmentation via global and local refinement. In *Proceedings of the IEEE/CVF Conference on Computer Vision and Pattern Recognition*, pages 8890–8899, 2020. 6
- [8] Zijun Deng, Xiaowei Hu, Lei Zhu, Xuemiao Xu, Jing Qin, Guoqiang Han, and Pheng-Ann Heng. R3net: Recurrent residual refinement network for saliency detection. In *Pro-*

- ceedings of the 27th International Joint Conference on Artificial Intelligence*, pages 684–690. AAAI Press Menlo Park, CA, USA, 2018. 10, 12
- [9] Xiaohan Ding, Xiangyu Zhang, Jungong Han, and Guiguang Ding. Scaling up your kernels to 31x31: Revisiting large kernel design in cnns. In *Proceedings of the IEEE/CVF Conference on Computer Vision and Pattern Recognition*, pages 11963–11975, 2022. 5
- [10] Deng-Ping Fan, Ming-Ming Cheng, Yun Liu, Tao Li, and Ali Borji. Structure-measure: A new way to evaluate foreground maps. In *Proceedings of the IEEE international conference on computer vision*, pages 4548–4557, 2017. 6, 7
- [11] Deng-Ping Fan, Cheng Gong, Yang Cao, Bo Ren, Ming-Ming Cheng, and Ali Borji. Enhanced-alignment measure for binary foreground map evaluation. *arXiv preprint arXiv:1805.10421*, 2018. 6
- [12] Deng-Ping Fan, Jing Zhang, Gang Xu, Ming-Ming Cheng, and Ling Shao. Salient objects in clutter. *IEEE Transactions on Pattern Analysis and Machine Intelligence*, 2022. 9, 10
- [13] Chaowei Fang, Haibin Tian, Dingwen Zhang, Qiang Zhang, Jungong Han, and Junwei Han. Densely nested top-down flows for salient object detection. *Science China Information Sciences*, 65(8):182103, 2022. 3
- [14] Mengyang Feng, Huchuan Lu, and Errui Ding. Attentive feedback network for boundary-aware salient object detection. In *Proceedings of the IEEE/CVF conference on computer vision and pattern recognition*, pages 1623–1632, 2019. 1, 3, 10, 12
- [15] Kaiming He, Xiangyu Zhang, Shaoqing Ren, and Jian Sun. Deep residual learning for image recognition. In *Proceedings of the IEEE conference on computer vision and pattern recognition*, pages 770–778, 2016. 6
- [16] Qibin Hou, Ming-Ming Cheng, Xiaowei Hu, Ali Borji, Zhuowen Tu, and Philip HS Torr. Deeply supervised salient object detection with short connections. In *Proceedings of the IEEE conference on computer vision and pattern recognition*, pages 3203–3212, 2017. 2, 10, 12
- [17] Bowen Jiang, Lihe Zhang, Huchuan Lu, Chuan Yang, and Ming-Hsuan Yang. Saliency detection via absorbing markov chain. In *Proceedings of the IEEE international conference on computer vision*, pages 1665–1672, 2013. 2
- [18] Lei Ke, Mingqiao Ye, Martin Danelljan, Yifan Liu, Yu-Wing Tai, Chi-Keung Tang, and Fisher Yu. Segment anything in high quality. *arXiv preprint arXiv:2306.01567*, 2023. 2
- [19] Yun Yi Ke and Takahiro Tsubono. Recursive contour-saliency blending network for accurate salient object detection. In *Proceedings of the IEEE/CVF Winter Conference on Applications of Computer Vision*, pages 2940–2950, 2022. 4, 10
- [20] Taehun Kim, Kunhee Kim, Joonyeong Lee, Dongmin Cha, Jiho Lee, and Daijin Kim. Revisiting image pyramid structure for high resolution salient object detection. In *Proceedings of the Asian Conference on Computer Vision*, pages 108–124, 2022. 7
- [21] Alexander Kirillov, Eric Mintun, Nikhila Ravi, Hanzi Mao, Chloe Rolland, Laura Gustafson, Tete Xiao, Spencer Whitehead, Alexander C Berg, Wan-Yen Lo, et al. Segment anything. *arXiv preprint arXiv:2304.02643*, 2023. 2
- [22] Guanbin Li and Yizhou Yu. Visual saliency detection based on multiscale deep cnn features. *IEEE transactions on image processing*, 25(11):5012–5024, 2016. 9
- [23] Long Li, Junwei Han, Nian Liu, Salman Khan, Hisham Cholakkal, Rao Muhammad Anwer, and Fahad Shahbaz Khan. Robust perception and precise segmentation for scribble-supervised rgb-d saliency detection. *IEEE Transactions on Pattern Analysis and Machine Intelligence*, 2023. 3
- [24] Xin Li, Fan Yang, Hong Cheng, Wei Liu, and Dinggang Shen. Contour knowledge transfer for salient object detection. In *Proceedings of the european conference on computer vision (ECCV)*, pages 355–370, 2018. 10, 12
- [25] Yin Li, Xiaodi Hou, Christof Koch, James M Rehg, and Alan L Yuille. The secrets of salient object segmentation. In *Proceedings of the IEEE conference on computer vision and pattern recognition*, pages 280–287, 2014. 9
- [26] Zun Li, Congyan Lang, Jun Hao Liew, Yidong Li, Qibin Hou, and Jiashi Feng. Cross-layer feature pyramid network for salient object detection. *IEEE Transactions on Image Processing*, 30:4587–4598, 2021. 2
- [27] Jun Hao Liew, Scott Cohen, Brian Price, Long Mai, and Jiashi Feng. Deep interactive thin object selection. In *Proceedings of the IEEE/CVF Winter Conference on Applications of Computer Vision*, pages 305–314, 2021. 12, 15
- [28] Tsung-Yi Lin, Piotr Dollár, Ross Girshick, Kaiming He, Bharath Hariharan, and Serge Belongie. Feature pyramid networks for object detection. In *Proceedings of the IEEE conference on computer vision and pattern recognition*, pages 2117–2125, 2017. 2, 4
- [29] Jiang-Jiang Liu, Qibin Hou, Ming-Ming Cheng, Jiashi Feng, and Jianmin Jiang. A simple pooling-based design for real-time salient object detection. In *Proceedings of the IEEE/CVF conference on computer vision and pattern recognition*, pages 3917–3926, 2019. 1, 2, 3, 10, 12
- [30] Nian Liu, Junwei Han, and Ming-Hsuan Yang. Picanet: Pixel-wise contextual attention learning for accurate saliency detection. *IEEE Transactions on Image Processing*, 29:6438–6451, 2020. 3, 7, 10, 12
- [31] Nian Liu, Ni Zhang, Ling Shao, and Junwei Han. Learning selective mutual attention and contrast for rgb-d saliency detection. *IEEE Transactions on Pattern Analysis and Machine Intelligence*, 44(12):9026–9042, 2021. 3
- [32] Nian Liu, Ni Zhang, Kaiyuan Wan, Ling Shao, and Junwei Han. Visual saliency transformer. In *Proceedings of the IEEE/CVF international conference on computer vision*, pages 4722–4732, 2021. 10
- [33] Ze Liu, Yutong Lin, Yue Cao, Han Hu, Yixuan Wei, Zheng Zhang, Stephen Lin, and Baining Guo. Swin transformer: Hierarchical vision transformer using shifted windows. In *Proceedings of the IEEE/CVF international conference on computer vision*, pages 10012–10022, 2021. 6
- [34] Shijian Lu, Cheston Tan, and Joo-Hwee Lim. Robust and efficient saliency modeling from image co-occurrence histograms. *IEEE transactions on pattern analysis and machine intelligence*, 36(1):195–201, 2013. 2

- [35] Wenjie Luo, Yujia Li, Raquel Urtasun, and Richard Zemel. Understanding the effective receptive field in deep convolutional neural networks. *Advances in neural information processing systems*, 29, 2016. [5](#)
- [36] Zhiming Luo, Akshaya Mishra, Andrew Achkar, Justin Eichel, Shaozi Li, and Pierre-Marc Jodoin. Non-local deep features for salient object detection. In *Proceedings of the IEEE Conference on computer vision and pattern recognition*, pages 6609–6617, 2017. [10](#), [12](#)
- [37] Jun Ma and Bo Wang. Segment anything in medical images. *arXiv preprint arXiv:2304.12306*, 2023. [2](#)
- [38] Ran Margolin, Lihi Zelnik-Manor, and Ayellet Tal. How to evaluate foreground maps? In *Proceedings of the IEEE conference on computer vision and pattern recognition*, pages 248–255, 2014. [6](#)
- [39] Sina Mohammadi, Mehrdad Noori, Ali Bahri, Sina Ghofrani Majelan, and Mohammad Havaei. Cagnet: Content-aware guidance for salient object detection. *Pattern Recognition*, 103:107303, 2020. [2](#), [10](#)
- [40] Robert Osserman. The isoperimetric inequality. *Bulletin of the American Mathematical Society*, 84(6):1182–1238, 1978. [15](#)
- [41] Youwei Pang, Xiaoqi Zhao, Lihe Zhang, and Huchuan Lu. Multi-scale interactive network for salient object detection. In *Proceedings of the IEEE/CVF conference on computer vision and pattern recognition*, pages 9413–9422, 2020. [3](#), [10](#), [12](#)
- [42] Adam Paszke, Sam Gross, Francisco Massa, Adam Lerer, James Bradbury, Gregory Chanan, Trevor Killeen, Zeming Lin, Natalia Gimelshein, Luca Antiga, et al. Pytorch: An imperative style, high-performance deep learning library. *Advances in neural information processing systems*, 32, 2019. [6](#)
- [43] Federico Perazzi, Jordi Pont-Tuset, Brian McWilliams, Luc Van Gool, Markus Gross, and Alexander Sorkine-Hornung. A benchmark dataset and evaluation methodology for video object segmentation. In *Proceedings of the IEEE conference on computer vision and pattern recognition*, pages 724–732, 2016. [12](#), [15](#)
- [44] Xuebin Qin, Hang Dai, Xiaobin Hu, Deng-Ping Fan, Ling Shao, and Luc Van Gool. Highly accurate dichotomous image segmentation. In *European Conference on Computer Vision*, pages 38–56. Springer, 2022. [4](#), [6](#), [7](#), [12](#), [13](#), [15](#)
- [45] Xuebin Qin, Zichen Zhang, Chenyang Huang, Masood Dehghan, Osmar R Zaiane, and Martin Jagersand. U2-net: Going deeper with nested u-structure for salient object detection. *Pattern recognition*, 106:107404, 2020. [2](#), [3](#), [4](#), [7](#), [8](#), [10](#)
- [46] Xuebin Qin, Zichen Zhang, Chenyang Huang, Chao Gao, Masood Dehghan, and Martin Jagersand. Basnet: Boundary-aware salient object detection. In *Proceedings of the IEEE/CVF conference on computer vision and pattern recognition*, pages 7479–7489, 2019. [1](#), [3](#), [10](#), [12](#)
- [47] Olaf Ronneberger, Philipp Fischer, and Thomas Brox. U-net: Convolutional networks for biomedical image segmentation. In *International Conference on Medical image computing and computer-assisted intervention*, pages 234–241. Springer, 2015. [2](#), [4](#)
- [48] David E Rumelhart, Geoffrey E Hinton, and Ronald J Williams. Learning representations by back-propagating errors. *nature*, 323(6088):533–536, 1986. [6](#)
- [49] Xiaoyong Shen, Xin Tao, Hongyun Gao, Chao Zhou, and Jiaya Jia. Deep automatic portrait matting. In *Computer Vision–ECCV 2016: 14th European Conference, Amsterdam, The Netherlands, October 11–14, 2016, Proceedings, Part I 14*, pages 92–107. Springer, 2016. [10](#)
- [50] Karen Simonyan and Andrew Zisserman. Very deep convolutional networks for large-scale image recognition. *arXiv preprint arXiv:1409.1556*, 2014. [9](#)
- [51] Jinming Su, Jia Li, Yu Zhang, Changqun Xia, and Yonghong Tian. Selectivity or invariance: Boundary-aware salient object detection. In *Proceedings of the IEEE/CVF International Conference on Computer Vision*, pages 3799–3808, 2019. [3](#), [10](#), [12](#)
- [52] Zhengzheng Tu, Yan Ma, Chenglong Li, Jin Tang, and Bin Luo. Edge-guided non-local fully convolutional network for salient object detection. *IEEE transactions on circuits and systems for video technology*, 31(2):582–593, 2020. [1](#)
- [53] Lijun Wang, Huchuan Lu, Yifan Wang, Mengyang Feng, Dong Wang, Baocai Yin, and Xiang Ruan. Learning to detect salient objects with image-level supervision. In *Proceedings of the IEEE conference on computer vision and pattern recognition*, pages 136–145, 2017. [9](#)
- [54] Tiantian Wang, Ali Borji, Lihe Zhang, Pingping Zhang, and Huchuan Lu. A stagewise refinement model for detecting salient objects in images. In *Proceedings of the IEEE international conference on computer vision*, pages 4019–4028, 2017. [10](#), [12](#)
- [55] Tiantian Wang, Lihe Zhang, Shuo Wang, Huchuan Lu, Gang Yang, Xiang Ruan, and Ali Borji. Detect globally, refine locally: A novel approach to saliency detection. In *Proceedings of the IEEE conference on computer vision and pattern recognition*, pages 3127–3135, 2018. [10](#), [12](#)
- [56] Andrew B Watson. Perimetric complexity of binary digital images: Notes on calculation and relation to visual complexity. Technical report, 2011. [15](#)
- [57] Jun Wei, Shuhui Wang, and Qingming Huang. F³net: fusion, feedback and focus for salient object detection. In *Proceedings of the AAAI Conference on Artificial Intelligence*, volume 34, pages 12321–12328, 2020. [2](#), [10](#), [13](#)
- [58] Jun Wei, Shuhui Wang, Zhe Wu, Chi Su, Qingming Huang, and Qi Tian. Label decoupling framework for salient object detection. In *Proceedings of the IEEE/CVF conference on computer vision and pattern recognition*, pages 13025–13034, 2020. [1](#), [4](#), [8](#), [10](#), [13](#)
- [59] Zhe Wu, Li Su, and Qingming Huang. Cascaded partial decoder for fast and accurate salient object detection. In *Proceedings of the IEEE/CVF conference on computer vision and pattern recognition*, pages 3907–3916, 2019. [3](#), [10](#), [12](#), [13](#)
- [60] Zhe Wu, Li Su, and Qingming Huang. Stacked cross refinement network for edge-aware salient object detection. In *Proceedings of the IEEE/CVF international conference on computer vision*, pages 7264–7273, 2019. [1](#), [4](#), [10](#), [12](#), [13](#)

- [61] Chenxi Xie, Changqun Xia, Mingcan Ma, Zhirui Zhao, Xiaowu Chen, and Jia Li. Pyramid grafting network for one-stage high resolution saliency detection. In *Proceedings of the IEEE/CVF Conference on Computer Vision and Pattern Recognition*, pages 11717–11726, 2022. 3, 12, 13, 15
- [62] Saining Xie and Zhuowen Tu. Holistically-nested edge detection. In *Proceedings of the IEEE international conference on computer vision*, pages 1395–1403, 2015. 4
- [63] Qiong Yan, Li Xu, Jianping Shi, and Jiaya Jia. Hierarchical saliency detection. In *Proceedings of the IEEE conference on computer vision and pattern recognition*, pages 1155–1162, 2013. 9
- [64] Chenglin Yang, Yilin Wang, Jianming Zhang, He Zhang, Zhe Lin, and Alan Yuille. Meticulous object segmentation. *arXiv preprint arXiv:2012.07181*, 2020. 15
- [65] Chuan Yang, Lihe Zhang, Huchuan Lu, Xiang Ruan, and Ming-Hsuan Yang. Saliency detection via graph-based manifold ranking. In *Proceedings of the IEEE conference on computer vision and pattern recognition*, pages 3166–3173, 2013. 1, 2, 9
- [66] Yi Ke Yun and Weisi Lin. Selfreformer: Self-refined network with transformer for salient object detection. *arXiv preprint arXiv:2205.11283*, 2022. 10
- [67] Yi Zeng, Pingping Zhang, Jianming Zhang, Zhe Lin, and Huchuan Lu. Towards high-resolution salient object detection. In *Proceedings of the IEEE/CVF International Conference on Computer Vision*, pages 7234–7243, 2019. 12, 15
- [68] Lu Zhang, Ju Dai, Huchuan Lu, You He, and Gang Wang. A bi-directional message passing model for salient object detection. In *Proceedings of the IEEE conference on computer vision and pattern recognition*, pages 1741–1750, 2018. 10, 12
- [69] Pingping Zhang, Dong Wang, Huchuan Lu, Hongyu Wang, and Xiang Ruan. Amulet: Aggregating multi-level convolutional features for salient object detection. In *Proceedings of the IEEE international conference on computer vision*, pages 202–211, 2017. 2, 10, 12
- [70] Qiang Zhang, Tonglin Xiao, Nianchang Huang, Dingwen Zhang, and Jungong Han. Revisiting feature fusion for rgb-t salient object detection. *IEEE Transactions on Circuits and Systems for Video Technology*, 31(5):1804–1818, 2020. 3
- [71] Hengshuang Zhao, Jianping Shi, Xiaojuan Qi, Xiaogang Wang, and Jiaya Jia. Pyramid scene parsing network. In *Proceedings of the IEEE conference on computer vision and pattern recognition*, pages 2881–2890, 2017. 2, 4, 8
- [72] Jia-Xing Zhao, Jiang-Jiang Liu, Deng-Ping Fan, Yang Cao, Jufeng Yang, and Ming-Ming Cheng. Egnet: Edge guidance network for salient object detection. In *Proceedings of the IEEE/CVF international conference on computer vision*, pages 8779–8788, 2019. 1, 2, 3, 10, 12
- [73] Xiaoqi Zhao, Youwei Pang, Lihe Zhang, Huchuan Lu, and Lei Zhang. Suppress and balance: A simple gated network for salient object detection. In *European conference on computer vision*, pages 35–51. Springer, 2020. 3, 10
- [74] Huajun Zhou, Xiaohua Xie, Jian-Huang Lai, Zixuan Chen, and Lingxiao Yang. Interactive two-stream decoder for accurate and fast saliency detection. In *Proceedings of the IEEE/CVF conference on computer vision and pattern recognition*, pages 9141–9150, 2020. 1, 4, 10
- [75] Mingchen Zhuge, Deng-Ping Fan, Nian Liu, Dingwen Zhang, Dong Xu, and Ling Shao. Salient object detection via integrity learning. *IEEE Transactions on Pattern Analysis and Machine Intelligence*, 2022. 3, 10, 13